Finanziato dall'Unione europea NextGenerationEU | Ministero dell'Università e della Ricerca | Italiadomani PIANO NAZIONALE DI RIPRESA E RESILIENZA

multi-Risk sciEnce for resilienT commUnities undeR a changiNg climate

Codice progetto MUR: **PE00000005**

Deliverable title: **Procedures for integration of in-situ systems and SAR interferometry for monitoring of critical infrastructures and for definition of alarm thresholds of early warning system**

Deliverable ID: **DV4.5**

Due date: **M38 (02/2026)**

Submission date: **28/02/2026**

AUTHORS

Raffaele Landolfo (UNINA), Maria Giuseppina Limongelli (POLIMI), Francesca Da Porto (UNIPD), Anna Saetta (IUAV), Andrea Miano (UNINA), Aldo Milone (UNINA), Pier Francesco Giordano (POLIMI), Elisa Saler (UNIPD), Marco Donà (UNIPD), Diego Talledo (IUAV), Fabrizio Aloschi (UNINA), Riccardo Liuzzo (POLIMI), Amedeo Caprino (UNIPD), Pietro Carpanese (UNIPD), Vincenzo Massimi (PLANETEK), Teresa Fazio (PLANETEK), Marina Zingaro (PLANETEZ), Raffaele Nutricato (GAP), Davide Oscar Nitti (GAP), Alessandro Parisi (GAP)

Approved by Marco Savoia (WP4 Leader)

1. Technical references

Project Acronym	RETURN
Project Title	multi-Risk sciEnce for resilienT commUnities undeR a changiNg climate
Project Coordinator	Domenico Calcaterra UNIVERSITA DEGLI STUDI DI NAPOLI FEDERICO II domcalca@unina.it
Project Duration	December 2022 – April 2026 (40 months)

Deliverable No.	DV4.5
Dissemination level*	PP
Work Package	WP4 – Modelling and experimental technologies (including AI) for vulnerability assessment
Task	T4.5 – SAR interferometry and remote sensing for deformation control
Lead beneficiary	UNINA
Contributing beneficiary/ies	POLIMI, UNIPD, ENGINEERING, IUAV, PLANETEK, GAP

* PU = Public

PP = Restricted to other programme participants (including the Commission Services)

RE = Restricted to a group specified by the consortium (including the Commission Services)

CO = Confidential, only for members of the consortium (including the Commission Services)

1.1 Document history

Version	Date	Lead contributor	Description
0.1	01.10.2024	Raffaele Landolfo (UNINA)	Table of contents
0.2	20.02.2026	Raffaele Landolfo (UNINA) Andrea Miano (UNINA) Aldo Milone (UNINA) Maria Giuseppina Limongelli (POLIMI) Pier Francesco Giordano (POLIMI) Francesca Da Porto (UNIPD) Elisa Saler (UNIPD) Anna Saetta (IUAV) Diego Talledo (IUAV) Vincenzo Massimi (PLANETEK) Raffaele Nutricato (GAP)	Critical review and proofreading
0.3	25.02.2026	All the Authors	Edits for approval
1.0	27.02.2026	All the Authors	Final version

2. ABSTRACT

Work Package 4 (WP4) addresses advanced technologies to evaluate the vulnerability of existing infrastructures, at the component level. Transportation, hydraulic and energy/telecommunication infrastructures are treated accounting for their different peculiarities. To this end, remote sensing techniques play a crucial role among research activities carried out within WP4.

In this framework, Synthetic Aperture Radar (SAR) Interferometry is the key topic addressed in Task 4.5, which is devoted to deformation control of Critical Infrastructures (CIs) through SAR data. Moreover, a strong focus is given to integration of in-situ structural health monitoring (SHM) – which is addressed in other Tasks within WP4 – with SAR-based remote monitoring, i.e., with the aim of defining some reliable criteria for early warning purposes.

In particular, this deliverable first deals with post-processing of satellite images and subsequent data extraction for SHM purposes. Different techniques for manipulation of SAR data are hence presented, i.e., including the filtering of environmental effects and the introduction of suitable statistical models for satellite image analysis (§5 and §6).

Subsequently, different rapid approaches based on InSAR monitoring are introduce to provide a large-scale risk classification for bridges belonging to critical infrastructural networks. After discussing related methodological aspects, some relevant applications are developed with reference to three POCs developed within the EP RETURN Project (Tirano-Milano-Marghera corridor, SS51 Alemagna roadway, Calabria Tyrrhenian coastline transportation network - §7).

Finally, key insights concerning integration of in-situ and space-borne SHM are discussed in §8.

3. Table of contents

3.1 List of Tables

3.2 List of Figures

4. Introduction

4.1 Background and motivation

Critical infrastructures, e.g. transport, industrial and power grid infrastructures are essential for ensuring the safety and socio-economic growth of communities. Nevertheless, existing CIs are often outdated and vulnerable. In past times, most efforts from research and technical practice were devoted to find suitable retrofit interventions for maintenance of damaged CIs. However, this approach proved to be occasionally ineffective as structural upgrading was only performed after damaging events (e.g., aftermaths from long-term ground motions – slow landslides, subsidence – or from extreme events such as strong earthquakes). As a result, severe losses in terms of repairing costs and temporary inoperability were sometimes achieved.

In response to such criticalities, SHM techniques have emerged in recent times to monitor the maintenance status of CIs and hence preserve their operability in an effective way. Historically, SHM first developed in the form of in-situ monitoring techniques, which involved the installation of different types of sensors to estimate displacements, deformations, vibrations, etc. in structural members belonging to CIs and/or to assess the evolution of degradation phenomena (e.g., carbonatation, corrosion, etc.). Subsequently, remote sensing techniques – which previously found their main field of application in aerospace and military purposes – were extended to civil engineering applications and SHM.

Within this framework, innovative remote sensing space-borne methods based on Synthetic Aperture Radar (SAR) image processing recently proved to be a great tool for monitoring deformations of extended areas, urban settlements, and single constructions. Several recent works regarding the use of remote sensing satellite data and their processing through Differential SAR Interferometry (DInSAR) techniques can be now found in literature, although this topic still acts as an open and fruitful field of research.

Namely, the use of SAR data requires some preliminary operations devoted to make raw satellite images suitable for SHM applications.

In this regard, different aspects are still under investigation nowadays. For instance, the quality of satellite images often proves to be sensibly affected by environmental effects, i.e., such as ambient noise, atmospheric disturbances and topography-related effects. Therefore, appropriate filtering algorithms are under development to address this issue. Moreover, even in presence of correctly filtered images, relevant information from SAR data still cannot be inferred unless reliable and robust statistical interpretative models are used. Also in this case, several approaches are being proposed in scientific literature. The above aspects constitute the core topic of DV4.5a document.

4.2 Outline of the report

The present report is divided in three main parts. Namely, techniques for filtering environment effects in SAR data are discussed in Section 5. Subsequently, statistical models to interpret filtered SAR data for CIs assessment are addressed in Section 6. Finally, main conclusive remarks drawn from dealt topics are summarized in Section 9. Each of the following Sections is articulated in the following subSections: 1) motivation (novelty, importance the addressed topic), 2) Literature review (and research gaps), 3) Methodology and 4) Demonstration.

5. Filtering of environmental effects in SAR data

5.1 Introduction

Bridges are vital components of transportation networks and are constantly exposed to degradation and hazards, putting their structural integrity at risk. Traditional bridge assessments rely on periodic inspections, which, while helpful, do not provide real-time data. Structural Health Monitoring (SHM) systems, which typically rely on contact sensors, can offer continuous, real-time insights into structural conditions. However, SHM systems are typically costly to install and maintain across large networks. Satellite-based Synthetic Aperture Radar Interferometry (InSAR) presents a cost-effective alternative, enabling millimetre-accurate displacement monitoring without the need for on-site sensors [1,2]. InSAR algorithms generate time series data at specific Measurement Points (MPs), which include Persistent Scatterers (PSs) and Distributed Scatterers (DSs), allowing for both localized and regional analysis of bridge conditions [3,4]. They can also allow investigating the past behaviour of structures and tracking of long-term structural trends [5,6] through the analysis of historical data.

To improve spatial and temporal analysis of displacements, multi-temporal InSAR (MT-InSAR) techniques have been developed. Newer SAR missions have further enhanced these capabilities improving infrastructure monitoring. The European Space Agency's European Ground Motion Service (EGMS), implemented in 2022 as part of the Copernicus program, processes Sentinel-1 data to monitor ground deformations across Europe and provides free of charge and user-friendly access to annual updates through a dedicated portal [7].

This section focuses on the monitoring of the Borgoforte Bridge in Italy, utilizing data from the EGMS portal and the COSMO-SkyMed (CSK) satellite constellation. The analysis compares the reconstructed structural displacements obtained from these datasets, discussing their respective strengths and limitations. Additionally, the influence of environmental effects on the bridge's structural behaviour is examined.

5.2 InSAR data processing

SAR satellites operate in both ascending and descending orbits. The method used in this work combines data from these orbits to reconstruct the horizontal component in the west-east direction and the vertical component of the structural displacement under the assumption that displacements in the north-south direction are negligible. This assumption is motivated by the low sensitivity of SAR satellites measurements to motion in that direction. The procedure includes the following key steps: (1) selection and clustering of MPs in predefined structural portions, (2) baseline removal, (3) computation of the mean displacements, (4) data resampling, and finally, (5) combination of the ascending and descending datasets [2]. The first phase involves selecting MPs from the dataset, filtering them based on the geographical coordinates of the bridge, and excluding points that are unlikely to belong to the bridge deck based on their location. The remaining MPs are then clustered into the predefined structural portions to identify displacement trends. To eliminate any offsets in the detected velocity values, the first recorded value is subtracted from all subsequent values in each time series. This standardization step ensures that all the time series start from a common reference point.

Next, the displacements of the MPs within the same cluster are averaged and temporal resampling is applied to the ascending and descending datasets to align acquisitions, which may occur on different days for the two orbits. Linear interpolation is used for this purpose in this work.

The displacement along the LoS (Line of Sight) can be described as a linear combination of the components of the displacement in the west-east (E), d_E, south-north (N), d_N, and vertical (U), d_U, directions, according

to the direction cosines of the LoS associated with the ascending (A) and to the descending (D) orbits. Assuming negligible displacement in the N direction, the following system of two equations in two unknowns is formulated:

$$\begin{cases} d_{LOS,A} \cong d_E \cos(\alpha_{E,A}) + d_U \cos(\alpha_{U,A}) \\ d_{LOS,D} \cong d_E \cos(\alpha_{E,D}) + d_U \cos(\alpha_{U,D}) \end{cases} \quad [1]$$

where $cos(\alpha_{E,A/D})$ and $cos(\alpha_{U,A/D})$ are the direction cosines of the LoS and $d_{LoS,A}$ and $d_{LoS,D}$ are the LoS displacements. By solving system [1], it is possible to determine the displacements in the E and U directions through the following relationships:

$$\begin{cases} d_E = k[cos(\alpha_{U,A})\, d_{LoS,D} + cos(\alpha_{U,D}) d_{LoS,A}] \\ d_U = k[cos(\alpha_{E,D})\, d_{LoS,A} - cos(\alpha_{E,A})\, d_{LoS,D}] \end{cases} \quad [2]$$

where $k = [cos(\alpha_{U,A}) \cdot cos(\alpha_{E,D}) - cos(\alpha_{U,D}) \cdot cos(\alpha_{E,A})]^{-1}$.

5.3 Case study: The San Benedetto Po Bridge

The bridge (Figure 5-1) crosses the Po River near the municipality of Borgoforte in Mantua, North of Italy. It was built between 1964 and 1966 and served as a key regional infrastructure for decades. Spanning 613 m with a 7.5 m-wide carriageway (later reduced to 7.2 m after pavement widening), the bridge featured a mixed structure of reinforced concrete and steel. It was supported by nine rectangular piers, four of which located in the riverbed. Each pier rested on eight piles, 1.4 m in diameter, extending 17 to 23 m below the riverbed. The bridge's deck comprised regular 67 m spans, with two outer spans of 38.5 m. The structure also featured balanced cantilevers on bi-pendulum piers, with Gerber saddle spans of 10 m. Over time, the bridge faced significant damage from major floods in 1993 and 2000, as well as the 2012 earthquake, which led to temporary closures and reinforcements. Degradation ultimately led to its demolition, with work on a replacement bridge currently underway.

Figure 5-1 – San Benedetto Po bridge (East side).

5.4 InSAR data

To study the San Benedetto Po Bridge, datasets from two sources are utilized: the EGMS portal and the CSK constellation (Figure 5-2). In the EGMS database, four datasets relevant to the bridge and its surrounding area are identified, comprising two datasets with ascending data and two with descending data. For each orbit, the

dataset with the highest number of MPs available is selected for the calculations. These datasets cover the period from 2015 to 2018.

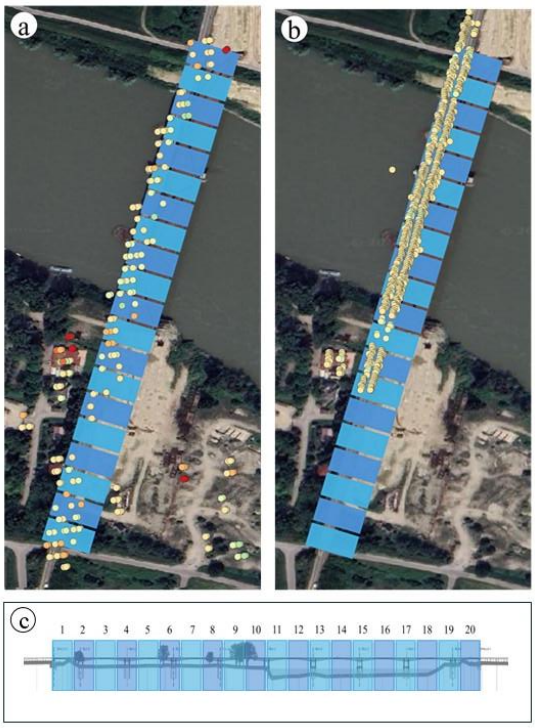

Figure 5-2 – Clustering of MPs into 20 areas: (a) EGMS data; (b) CSK data; (c) side view.

Regarding CSK data, two datasets are analyzed: one for ascending geometry and one for descending one. The algorithm used for processing satellite radar images is Coherent Pixels Technique (CPT), developed by [8] at the Remote Sensing Laboratory (RSLab) of the Universitat Politècnica de Catalunya (UPC) and implemented in the SUBSIDENCE software. This algorithm makes it possible to develop the entire interferometric chain using pairs of images with optimized spatial and temporal baselines and therefore characterized by a better phase response. In detail, the ascending dataset consists of 47 images, while the descending dataset consists of 51 images. The processing chain consists of three main phases:

(a) generation of the best interferograms from the available image dataset;

(b) selection of reflectors (PS) characterized by a fixed phase value considered indicative of good stability of the electromagnetic response;

(c) calculation of the average displacement velocities and the displacement time series of the selected points over the observation period considered.

Both datasets were imported into GIS software to facilitate spatial analysis and visualize the distribution of MPs across the Earth's surface, see Figure 5-2.

5.5 Results

5.5.1 Structural displacements

In this study, the analysis focuses on the vertical displacements of the bridge. InSAR data are processed according to the methodology presented in Section 5.2. Results are shown in Figure 5-3, where the mean displacement time series of the zones shown in Figure 5-2 are shown.

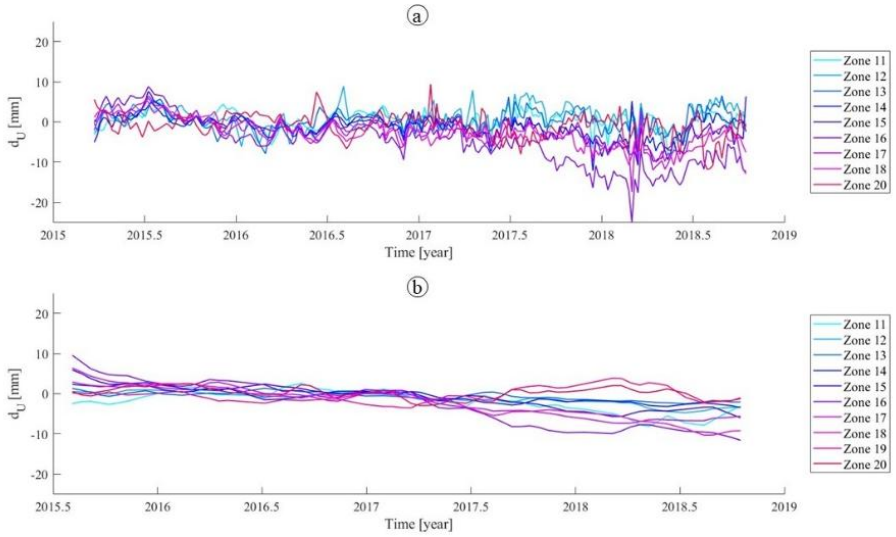

Figure 5-3 – Vertical displacements: (a) EGMS dataset; (b) CSK dataset.

As for the EGMS dataset, vertical displacements present irregular behavior with an overall negative slope. The range of displacements is between -25 mm and +10 mm, with some more marked oscillations especially towards the end of the observed period, around 2018. The CSK dataset, on the other hand, shows smoother variations with respect ot the EGMS dataset. In this case, the range of vertical displacements roughly lies between -10 mm and +10 mm, with a negative slope. No seasonal trend is observed both for EGMS/CSK data.

5.5.2 Correlation with environmental factors

In this section, the relationship between the reconstructed vertical displacements and the two environmental factors, i.e. air temperature and water level, is explored. These data were provided by the Agenzia Interregionale per il Fiume Po (AIPO). Pearson Correlation Coefficients (PCCs) were computed to quantify the influence of temperature (ρ_{UT}) and and water level (ρ_{UW}) on the structural displacements.

As shown in Table 5-1, the correlation between temperature and vertical displacements is generally weak in both datasets, with no clear trends emerging; this suggests that temperature variations do not significantly influence the observed vertical displacements.

Table 5-1 – PCCs between vertical displacements and environmental factors (temperature and water level) for both EGMS and CSK datasets.

	Zone	ρ_{UT} (EGMS)	ρ_{UW} (EGMS)	ρ_{UT} (CSK)	ρ_{UW} (CSK)
Access embankment	1	0.29	-0.30	-	-
	2	0.12	-0.21	-	-
	3	0.30	-0.23	-	-
	5	-0.16	-0.01	-	-
	8	-0.13	-0.27	-	-
	9	0.07	-0.37	-	-
	10	0.32	-0.49	-	-

Riverbed	11	0.01	-0.74	0.02	-0.51
	12	0.12	-0.59	0.52	-0.42
	13	0.01	-0.45	-0.16	-0.56
	14	-0.01	-0.50	0.46	0.03
	15	0.05	-0.57	-0.29	-0.32
	16	-0.24	-0.35	-0.08	0.20
	17	0.05	-0.46	-0.14	-0.06
	18	-0.22	-0.35	0.55	-0.00
	19	-	-	0.18	0.43

A stronger relationship is observed between vertical displacements and water level, particularly in the EGMS dataset. The first two columns show a significant negative correlation for several zones near the riverbed in the EGMS dataset, with Zone 11 displaying the strongest correlation ($\rho_{UW} = -0.736$). This indicates that higher water levels generally correspond to downward vertical movements. In contrast, the CSK dataset reveals weaker correlations, with several zones exhibiting near-zero or positive values, confirming the lower sensitivity of the dataset to water level changes. These findings are confirmed by the results in Figure 5-4, which displays the scatter plots of water level vs. vertical displacements. The figure reports the EGMS data for Zone 5 (access embankment) and Zone 11 (riverbed), the linear best fitting lines, and the associated coefficient of determination R2 values. For the CSK dataset, the scatter plot for water level vs vertical displacements in Zone 11, shown in Figure 5-5, reveals small R^2 and therefore no significant correlation, further highlighting the discrepancies between the two datasets. CSK results do not cover Zone 5.

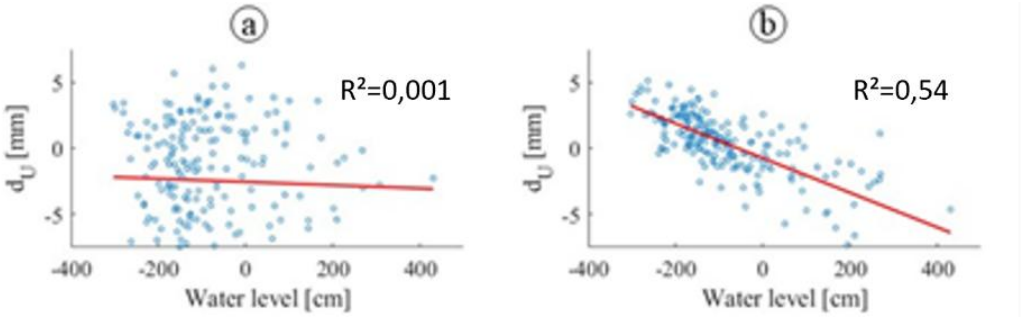

Figure 5-4 – Scatter plot of water level vs. vertical displacements for the EGMS dataset: (a) Zone 5 (access embankment); (b) Zone 11 (riverbed).

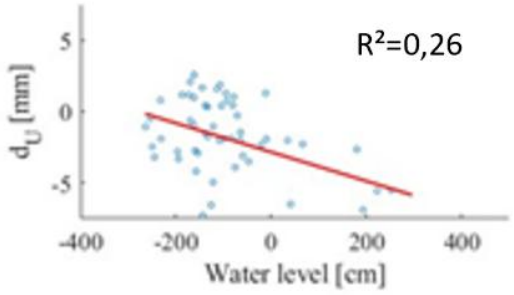

Figure 5-5 – Scatter plot of water level vs. vertical displacements in Zone 11 for the CSK dataset.

5.6 Conclusive remarks of this Section

This Section analysed the vertical displacements of the San Benedetto Po Bridge in Italy using data from two sources: the EGMS portal, which relies on Sentinel-1, and high-resolution data from the COSMO-SkyMed

(CSK) satellite constellation. Specifically, it investigated the correlation between InSAR vertical displacements and two environmental factors: temperature and water level of the Po River. The findings indicate that temperature has a negligible effect on the vertical displacement of the bridge, as shown by the weak correlation values in both datasets. In contrast, for the EGMS dataset, significant negative correlations were observed between vertical displacements and fluctuations in the river's water level, particularly for the portion of the bridge located in the riverbed. This correlation, however, was not present in the CSK data, raising concerns about potential measurement discrepancies, likely caused by data processing artifacts. Future work will aim to optimize various InSAR techniques for reconstructing structural displacements under varying environmental conditions. Additionally, further analysis will investigate displacement trends in both vertical and longitudinal directions, as well as potential torsional movements, to provide a more comprehensive understanding of the bridge's structural behavior.

6. Statistical models to interpret SAR data for CIs assessment

6.1 Introduction

Satellite interferometry has recently developed as a powerful tool for monitoring displacements on structures for structural health monitoring (SHM), as it allows obtaining information on past deformation and performing back analysis on structural behavior. Multi-Temporal InSAR methods (MT-InSAR) have recently assumed a relevant role in the analysis deformations of buildings and infrastructures by detecting displacement velocity of coherent points along the satellite line of sight (LOS), providing accurate time series [1-4]. Despite the increasing in literature on this subject, the lack of protocols for applying and interpreting interferometric data for structural assessment prevents these techniques from being employed alongside conventional SHM.

Among MT-InSAR techniques, Permanent Scatterers Interferometry (PS-InSAR) [5] and SBAS-DInSAR [6,7] methods have proven to be reliable in detecting ground motion and building displacements. Referring to SHM applications, MT-InSAR methods have proven able to detect displacement phenomena on infrastructures [8-11] and civil structures [2,12-14].

In this work, the proposed methodology for interpreting SAR data for CIs assessment focuses on the back monitoring analysis for recognition of past and recent deformation with increasing scale of analysis: starting from a territorial analysis of displacements, the protocol then switches to a single-structure scale. The back monitoring section investigates the possibility of applying algorithms and methods derived from conventional monitoring, such as detrending and damage detection algorithms, to interferometric data.

6.2 Processing SAR data for monitoring displacements

The SBAS-DInSAR (*Small BAseline Subset Differential Interferometry*) technique exploits a large number of satellite SAR images acquired on a selected area during a certain monitoring period: in detail, the primary purpose of SBAS-DInSAR is to correctly select pairs of satellite images characterized by both small perpendicular baseline (the distance between the position of two acquisition points of the satellite sensor along his orbital track) and small temporal baseline (the time interval between the acquisition of two satellite images), and obtain the phase difference between the same images in the so-called differential interferograms. Thus, the above-mentioned criteria enable the reduction of the noise effects on the multi-temporal series of differential interferograms and optimize the number of measurement points detected on earth. Later, the same interferograms undergo the unwrapping phase to solve the 2π phase ambiguities and to collect the original phase signal, and the displacement time series are defined by solving a linear system of equations in the least squares sense [15-18]. Last, a filtering process allows the removal of atmospheric effects from the time series.

The main outcome of this technique is the definition of measurement points spatially georeferenced (by longitude, latitude, and altitude) and supplied by the coherence measure (from 0 to 1), defining the stability of the target and its reliability, the mean annual LOS velocity value (given in mm/year) and the displacement time series over the monitoring period. SBAS-DInSAR technique provides measurements with an accuracy of 1–2 mm/year for LOS velocity values and 5/10 mm for each measure within the time series [19-23].

The method for data processing and monitoring is divided into three main sections: Background information, Pre-processing, and Back analysis [24]

6.2.1 Background information

The first part of the analysis begins by collecting principal information about the structure being monitored. Specifically, the constructive development and principal features of the structure are addressed, as well as the geometry and state of conservation. In this way, potential criticalities are investigated.

6.2.2 Pre-processing

Multi-interferometric data analysis starts with a primary analysis which evaluates the mean LOS displacement velocity (VLOS).

Urban scale analysis considers the whole satellite data and aims at highlighting areas characterized by the highest deformation rate inside the city. A brief statistical analysis is accomplished to recognize the distribution of VLOS values in the entire data. For a better comprehension of deformations, the pointwise distribution is transformed into a continuous map through a spatial interpolation approach, the Inverse-Distance-Weighting (IDW) technique [25]. Interpolation is carried out through quadratic weighting and by defining the AOI (Area Of Interest) inside a Geographical Information System (GIS) environment, such as QGIS [26], for both orbits. Interpolated maps are then used to estimate real displacement components, computed from a combination of ascending and descending data on pixels common to both maps. Vertical and east-west deformations are calculated through the following expressions (Eqs. 3 and 4).

$$V_{Vertical} = \frac{(V_{LOSdesc}/e_{desc}) - (V_{LOSasc}/e_{asc})}{\left(\frac{h_{desc}}{e_{desc}}\right) - \left(\frac{h_{asc}}{e_{asc}}\right)} \quad [3]$$

$$V_{E-W} = \frac{(V_{LOSdesc}/h_{desc}) - (V_{LOSasc}/h_{asc})}{\left(\frac{e_{desc}}{h_{desc}}\right) - \left(\frac{e_{asc}}{h_{asc}}\right)} \quad [4]$$

where $V_{LOSdesc}$, and V_{LOSasc} are the mean LOS displacement velocity, respectively, for descending and ascending orbits, while h and e are horizontal and vertical directional cosines of the respective orbit [27].

Single-structure scale examines the points distribution both from a planimetric and an elevation point of view. For the same purpose, real deformation components are now qualitatively detected through the use of single data: vertical and horizontal displacements are calculated by dividing ascending and descending LOS velocity values respectively by vertical and horizontal directional cosines, modifying the expressions defined by [28], as follows (Eqs. 5 and 6).

$$V_{Vertical,asc} = \frac{V_{LOSasc}}{h_{asc}}, V_{Vertical,desc} = \frac{V_{LOSdesc}}{h_{desc}} \quad [5]$$

$$V_{E-W,asc} = \frac{V_{LOSasc}}{e_{asc}}, V_{E-W,desc} = \frac{V_{LOSdesc}}{e_{desc}} \quad [6]$$

6.2.3 Back analysis

A preliminary analysis of time histories is performed to understand global displacements/rotations of the structure, provide initial information, and, mostly, observe the presence of deformational trends which may affect displacement series.

After the time series analysis, the correlation between environmental effects and recorded displacements is performed to evaluate the influence of external parameters on measured displacements [29-30]. Firstly,

displacement time series are resampled weekly to fill gaps within various time windows; later, for each date, a measure of average daily temperature is retrieved from local services.

Thus, the correlation between temperature and displacement analysis is evaluated through the Pearson coefficient [31], as for the following expression (Eq. 7).

$$r_{td} = cov(t,d)/(\sigma_t \sigma_d) \quad [7]$$

where t and d are temperatures and resampled displacement time series of a single MP, and σ_t and σ_d are the standard deviation of the two parameters [32,33].

Later, the whole analysis focuses on the most vulnerable parts of the structure, defined according to both the Pre-processing analysis and possible observed crack patterns. Cluster analysis is performed to locate structurally homogeneous MPs.

A seasonal detrending technique is then applied to remove the environmental component from displacement time series and detect irreversible and pure deformation. For this purpose, the simple moving average (SMA) method [34] is implemented following the following expression (Eq. 8).

$$SMA_m = \frac{P_m + P_m - 1 \ + \cdots + P_{m-(n-1)}}{n} \quad [8]$$

where P_m is the displacement value at instant m and n is the number of values included inside the mean calculation [35,36]. The preferred method is to use an annual moving average by applying n = 52 moving dates to obtain the displacement at instant m, which is determined by averaging an entire year of previous values to consider environmental and noise effects. The AutoRegressive output with an eXogenous input part model (ARX) is then employed for deeper analysis of trends recognition inside time series, but also to develop an automated damage detection system.

During the estimation phase, the model is built using the temperature dataset as input and LOS displacement as output. This process identifies an ideal displacement time series, which is then tested in the validation phase introducing the remaining part of the temperature data. Thus, uploading LOS displacement data of the validation period, residuals ek between the ideal model and real measured parameter are calculated and, starting from them, three coefficients are derived for the evaluation of the quality of the model: i) the goodness of fit [37], ii) the loss function λ_0 [38], and iii) the final prediction error (FPE) [39], showed in Equations 9, 10, 11, respectively.

$$GOF = \left(1 - \frac{\sqrt{\frac{\sum_{k=1}^{N} e_k^2}{N}}}{\bar{y}}\right)\% \quad [9]$$

$$\lambda_0 = \frac{1}{N}\sqrt{\sum_{k=1}^{N} e_k^2} \quad [10]$$

$$FPE = \lambda_0 \frac{1 + d/N}{1 - d/N} \quad [11]$$

Among all possible combinations between $[n_a, n_b, n_k]$ = [1:10, 1:10, 1:10], the best fitting ARX model is selected considering the highest *GOF*, the lowest λ_0, and the lowest *FPE*: comparing the model and the real

data, the first parameter evaluates the accuracy of the fitting while the others define the misfitting level. For detection of possible outliers, a confidence interval of 95% was set, with a range calculated as in Eq. 12.

$$[y - t_{\frac{\alpha}{2},\nu}\sigma_y; y + t_{\alpha/2,\nu}\sigma_y] \quad [12]$$

where *y* is the output value in the estimation phase, *t* represents the Student's T distribution of parameter y and σy is its standard deviation. Thus, if residuals remain inside the confidence interval, the structural condition is stable; conversely, if residuals exceed the confidence interval, an instability phenomenon may have occurred.

6.1 Conclusive remarks of this Section

In this Section, most used and reliable statistical models for interpretation of SAR data were discussed, i.e., with a peculiar focus on using such models for CIs monitoring.

Remarkably, insights about recollection of background information, pre-processing of multi-temporal interferometric data and back-analysis of results were provided.

Discussed formulations can be suitably used for large-scale analysis of CIs, i.e., as it will be shown in relevant subsequent Sections.

7. Large-scale assessment of transportation networks via InSAR monitoring

7.1 Generality

In this Section, a large-scale methodology for the preliminary structural assessment of critical bridge networks using satellite-derived deformation data is discussed and applied with reference to representative case-studies belonging to three different Proof of Concepts developed within the EP RETURN Project.

To this end, it is worth mentioning that in literature different approaches have been presented in the past, both for buildings and for infrastructures (e.g. [40-42]).

The proposed approach uses MT-DInSAR measurements from both ascending and descending orbits and hence analyses displacement trends of the measure points to derive a risk classification for in service bridges. For this purpose, different preliminary, yet rapid methodologies are introduced. This classification can help stakeholders to identify the most vulnerable infrastructures and hence develop more targeted monitoring and maintenance strategies.

7.1.1 Selected case studies

As mentioned above, three case studies belonging to POCs were selected for applications. Namely:

i) POC 2-1 consists on the road corridor between Tirano, Milano and Marghera (Venice). It comprises a road network of about 700 km and a total of about 480 bridges, including bridges that cross or provide access to the corridor, is considered in the analysis;

ii) POC 2-2 regards SS51 Alemagna, i.e., a roadway network crossing mountainous regions within provinces of Treviso, Belluno and Venice. The area is mainly prone to hydrogeological hazards such as landslide, debris flow and stream/river flood. InSAR techniques are therefore useful to integrate monitoring of both slopes and infrastructures;

iii) POC2-3 is located along the Tyrrhenian coastline in Calabria, Southern Italy. The implemented analyses at territorial scale of roadway and railway networks involved the definition of a georeferred grid corresponding to the footprint of each structure. The implemented bridge discretization then allows the clustering of Measurement Points (MPs).

7.2 Methodology

In the context of the POC2-1 an automatic and multi-level procedure has been adopted. The procedure does not require having at disposal surface geometries for each bridge representing its footprint, but requires at least one geo-referenced position (typically given in form of a point representing the bridge center).

Hence, leveraging available datasets like for instance the one available in OpenStreetMaps (OSM), a spatial join between the two datasets can be made obtaining as line segments the bridge dataset in the area of interest. These lines are subdivided into smaller segments with size equal to the grid that the user wants to consider. The size of the grid should be chosen considering the resolution of the InSAR data considered.

Finally an offset is performed on these geometries to obtain a grid discretization of the bridges in the considered AOI. This dataset of pixels can be finally merged with spatial join operations with the MPs dataset considered. More details can be found in [42].

In the context of the POC2-2, an automatic script was developed to extract a georeferred footprint for each bridge and to define a parametric discretization of the footprint grid. This script is designed to extract bridge-related infrastructure data from OpenStreetMap (OSM) using a spatial query based on a polygonal region of interest.

The goal is to process raw OSM data and transform it into geometric representations suitable for further geospatial analysis – i.e., particularly polygons that represent the full footprint or envelope of bridge structures. Raw OSM data represent bridges as segments and not as polygons (i.e., only the longitudinal axis is retrieved). These lines are then extended by 15% in length, to take into account also the bridge abutments that might be neglected by OSM. The script then constructs parallel lines to each bridge central line, with offsets is defined according to the road type.

Two procedures for discretization are then implemented, to compare the outcome clustering of MPs: *i*) in the first case, the script is designed to create a 30 × 30 m grid, i.e., with each tile covering the entire cross-section of the bridge; *ii*) the second procedure involved subdividing each bridge according to its longitudinal axis. The transverse section of the structure is thereby split into two distinguished tiles. In this case, dimensions of the tiles were reduced to form a 20 × 20 m grid.

In both cases, the script computes the number of tiles that fit along the bridge length and samples points along both the left and right offset lines. These points are paired up into quads, forming a quadrilateral tile. Lastly, the script enriches the grid cells by aggregating and analyzing InSAR data from EGMS. The main operation is a spatial join, checking which MPs fall within each grid tile.

Statistical analysis of each grid tile is performed, calculating the number of associated points and their density, mean velocity, and standard deviation.

Regarding POC2-3 area, located in Calabria, Southern Italy, the methodological approach is based on the deployment of analysis cells along the road's longitudinal axis, as illustrated in Figure 7-1.

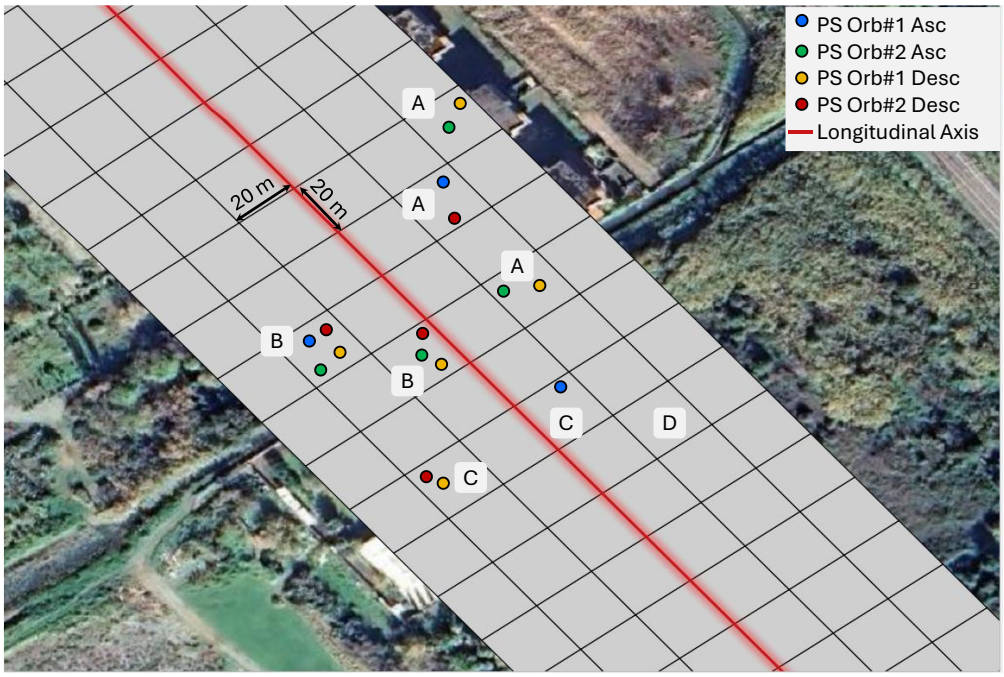

Figure 7-1 – Example of cell-based grid with 20-m spacing and lateral extension. Cases A–D illustrate different LOS measurement configurations from ascending and descending Sentinel-1 orbits.

The cells are deployed at regular 20-m intervals, extending three cells to the right and three to the left of the axis. This configuration is intended to investigate not only the road infrastructure itself but also the surrounding environment.

Shown points represent hypothetical positions of Persistent Scatterers (PS), i.e., each measuring displacement along its own Line of Sight (LOS). Two ascending and two descending satellite orbits are assumed, consistent with the actual Sentinel-1 acquisition geometry over POC2-3, giving rise to four possible configurations – Cases A, B, C, and D.

Case A depicts a situation where both ascending and descending measurements are available within the same cell. Under such conditions, it is theoretically possible [43-44] to combine the two measurements into a determined system of equations, enabling the retrieval of displacement components in the vertical and east directions. The examples of Case A demonstrate that having multiple ascending and descending orbits over the same area improves spatial coverage, as the number of valid combinations increases.

Case B presents a condition of information redundancy, where multiple ascending and descending acquisitions provide measurements within the same cell. This redundancy can be advantageously exploited to solve the resulting overdetermined system of equations, thus enhancing the robustness of vertical and east component estimations.

Case C shows a scenario where measurements are present but originate from a single acquisition pass (either ascending or descending). In this case, it is not possible to derive both east and vertical components, as the necessary diversity in look angles is missing.

Case D corresponds to a complete absence of measurement points within the cell. The availability of both vertical and east displacement components offers a substantial advantage in interpreting deformation phenomena that may affect bridges and roadway infrastructure. However, the absence of either ascending or descending acquisitions inhibits the derivation of these components.

Nevertheless, single-geometry line-of-sight measurements remain valuable, as they can capture relevant kinematic behaviours — including non-linear trends such as seasonal oscillations or progressive accelerations. An additional benefit of single-geometry data lies in the avoidance of integration and rasterization steps, since no combination with complementary passes is required. This enables point-wise analyses with enhanced geolocation accuracy in detecting the exact origin of observed displacements.

This motivates a hybrid approach in which all available acquisition geometries are first combined to derive vertical and eastward displacement components, i.e., rasterized into 20 m cells. Concurrently, single-geometry measurements are independently analysed to detect potential kinematic anomalies directly along the LOS.

It is important to note that LOS measurements represent only the projection of the true displacement vector along the radar line of sight. As such, they inherently underestimate the magnitude of the actual ground movement.

For the POC2-3 site, four distinct types of LOS-based kinematic hotspots were identified: *i*) Seasonality Hotspot: points where the amplitude of the seasonal displacement component exceeds a predefined threshold, suggesting cyclic behaviour potentially linked to environmental or structural factors; *ii*) Average Velocity Hotspot: points exhibiting a long-term average LOS velocity that exceeds a specified threshold, indicating persistent displacement over the full observation period; *iii*) Average Acceleration Hotspot: points characterized by a significant average acceleration of the displacement trend, pointing to non-linear evolution in the displacement dynamics over time; *iv*) Velocity Difference Hotspot: points where the LOS velocity in the

most recent year shows a notable increase (velocity difference) compared to the historical average, exceeding a defined threshold and suggesting newly emerging instabilities.

These hot spots are retrieved by computing flag values according to the following mathematical formulations (Eqs. 13-16):

$$Flag_S: f(x) = \begin{cases} 0, & SA_L < 3\ mm \\ 1, & 3\ mm \leq SA_L < 5\ mm \\ 2, & 5\ mm \leq SA_L < 10\ mm \\ 3, & SA_L > 10\ mm \end{cases} \quad [13]$$

$$Flag_V: f(x) = \begin{cases} 0, & |AVWP\_L| < 3\frac{mm}{year} \\ 1, & 3\frac{mm}{year} \leq |AVWP_L| < 5\frac{mm}{year} \\ 2, & 5\frac{mm}{year} \leq |AVWP_L| < 10\frac{mm}{year} \\ 3, & |AVWP_L| > 10\frac{mm}{year} \end{cases} \quad [14]$$

$$Flag_A: f(x) = \begin{cases} 0, & |AAWP\_L| < 1\frac{mm}{year^2} \\ 1, & 1\frac{mm}{year^2} \leq |AAWP_L| < 2\frac{mm}{year^2} \wedge sign(AAWP_L) = sign(AVWP_L) \\ 2, & 2\frac{mm}{year^2} \leq |AAWP_L| < 3\frac{mm}{year^2} \wedge sign(AAWP_L) = sign(AVWP_L) \\ 3, & |AAWP_L| > 3\frac{mm}{year^2} \wedge sign(AAWP_L) = sign(AVWP_L) \end{cases} \quad [15]$$

$$Flag_D: f(x) = \begin{cases} 0, & |\mathrm{AVRP_L} - AVWP_L| < 5\frac{mm}{year} \\ 1, & 5\frac{mm}{year} \leq |AAWP_L| < 10\frac{mm}{year} \wedge |AVRP_L| > |AVWP_L| \\ 2, & 10\frac{mm}{year} \leq |AAWP_L| < 20\frac{mm}{year} \wedge |AVRP_L| > |AVWP_L| \\ 3, & |AAWP_L| > 20\frac{mm}{year} \wedge |AVRP_L| > |AVWP_L| \end{cases} \quad [16]$$

where:

SA_L = Seasonal Amplitude (LOS); $AVWP_L$ = Average Velocity Whole Period (LOS); $AAWP_L$ = Average Acceleration Whole Period (LOS); $AVRP_L$ = Average Velocity Recent Period (LOS). Where "recent" refers to the last year of observation. Velocity estimates are obtained after removing the seasonal component from the time series.

After computing each flag, they can be easily aggregated into a global flag ($Flag_G$) using different strategies. Two possible approaches are presented hereinafter (Eqs. 17-18):

Weighted sum strategy

$$Flag_G = w_S \cdot Flag_S + w_V \cdot Flag_V + w_A \cdot Flag_A + w_D \cdot Flag_D \quad [17]$$

where w_S, w_V, w_A, w_D are weighting coefficients that can be tuned depending on the relevance assigned to each criterion.

Maximum strategy

$$Flag_G = \max\left(Flag_S, Flag_V, Flag_A, Flag_D\right) \quad [18]$$

For the proposed application to POC2, the maximum strategy was cautiously applied.

It is important to note that all these flags are computed individually for each available PS. These pointwise flags can be hence aggregated at 20 m cell-level via different strategies, such as *i*) computing the spatial average or *ii*) selecting the maximum value within each cell.

The choice of the most suitable aggregation method depends on the desired emphasis, i.e., on highlighting the severity of individual critical points rather than on representing the average condition of the entire cell.

For example, assuming that in a given cell there are N points for which all flags have been computed, denoted as $Flag_j(P_i)$ – where j indicates the flat type (S, V, A, D or G) and P_i indicates the i-th PS – the aggregation at the cell level can be performed through different techniques, such as (Eqs. 19-20):

Maximum aggregation technique

$$Flag_j(cell) = \max_{i=1,\dots,N} Flag_G(P_i) \quad [19]$$

Average aggregation technique

$$Flag_j(cell) = \frac{1}{N}\sum_{i=1}^{N} Flag_j(P_i) \quad [20]$$

where the first alternative (i.e., the one adopted for POC2 application) emphasizes the most critical behaviour within the cell, while the second one provides a representative average condition. The choice between these strategies depends on whether the analysis aims to highlight extreme local displacements or to characterize the overall condition of the area.

In order to provide a brief summary of discussed approaches, the overall workflow for SAR-based assessment of bridges is illustrated in Figure 7-2.

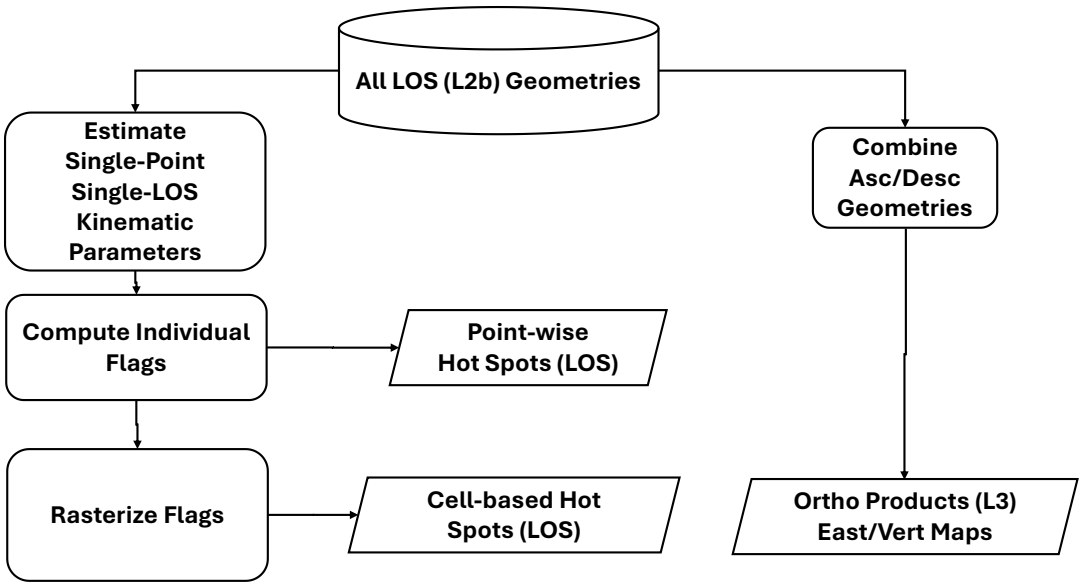

Figure 7-2 – Proposed workflow for large-scale SAR-based analysis of POC2.

7.3 Results and discussion

7.3.1 POC 2-1: Tirano-Milano-Marghera corridor

As mentioned previously, POC 2-1 case study consists on the road corridor between Tirano, Milano and Marghera (Venice). It comprises a road network of about 700 km and a total of about 480 bridges, including bridges that cross or provide access to the corridor, is considered in the analysis. A view of the corridor (in blue), indicating the considered bridges (in red), is represented in Figure 7-3.

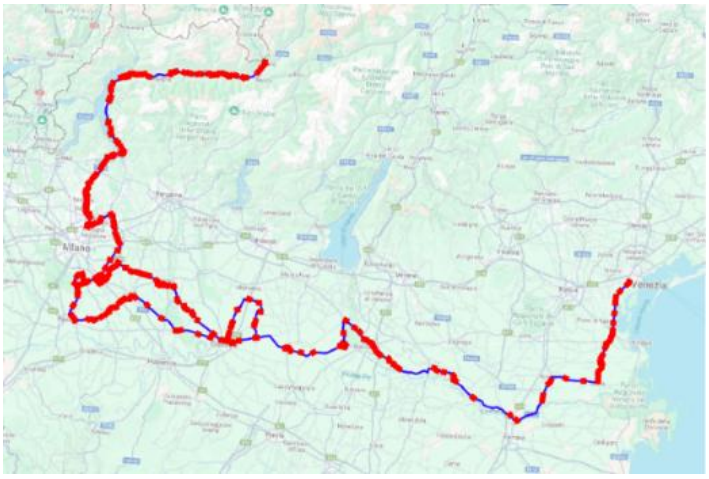

Figure 7-3 – Overview of POC2-1 Tirano-Milano-Marghera corridor (in blue). The selection of bridges considered in the analysis is highlighted in red.

The EGMS data for the three available time windows (2015-2021, 2018-2022, 2019-2023) have been considered for all available tracks (3 tracks ascending and 3 tracks descending) and the corresponding dataset of MPs have been merged with the grid pixels obtained by the discretization process.

Specifically, the bridges have been discretized with a 20 × 20 m regular grid. After the spatial join has been performed in terms of useful statistics on the MPs contained in each pixel grid (e.g. average, standard deviation, number of MPs), the available information on the different tracks has been used to compute vertical and east-west velocity components. Figure 7-4 depicts as an example the average annual vertical velocity computed for each cell of a bridge located north of Mantova.

Figure 7-4 – Example of merged InSAR data for a specific bridge near Mantova: mean vertical velocity computed for the 2015-2021 time window.

The total number of grid pixels that discretize the whole dataset of bridges is ≈3000. Out of these:

i) for about 300 pixels (i.e., about 10% of the pixels) no information is available for either ascending or descending orbits, therefore not allowing to perform any further analysis;

ii) For about 15% of the pixels only information relative to one orbit (ascending or descending) is available therefore non permitting to retrieve the vertical and east-west components;

iii) For another 10% of the pixels two tracks are available but of the same orbit, i.e., not permitting to compute the vertical and east-west components of velocity also in this case;

iv) For the remaining 60% of the pixels, information of both ascending and descending orbits are available and the vertical and east-west components can be computed correctly.

For instance, if more than one track for one (or both) of the orbits is available, multiple approaches could be followed for using this information: *a*) all the possible combinations selecting one ascending and one descending orbit could be considered, or *b*) (based on a quality index) the most reliable ascending and the most reliable descending orbit can be selected; finally, *c*) it is possible to merge all information solving the system of equations with a Weighted Least Squares approach in order to weight more the more reliable tracks [42].

After processing, for each grid pixel a set of multi-criteria flags is activated:

1. A mean vertical velocity higher than a threshold of 4 mm/yr;
2. A mean horizontal velocity higher than a threshold of 4 mm/yr;
3. An ascending mean velocity along the LOS higher than a threshold of 4 mm/yr;
4. A descending mean velocity along the LOS higher than a threshold of 4 mm/yr;
5. Variation with respect to last time window larger than 100% for each of the above mentioned data points.

It is worth noting that criterium #5 exploit the annual release of EGMS data, i.e., keeping track of significant differences in terms of mean annual velocity. For this last criterium, in order to account for possible large percentage differences, a lower threshold of 0.5 mm/yr is considered, i.e., below which the flag is not activated irrespective of the percentage difference.

Proposed thresholds can be considered as preliminary suggestions for a generic stock of bridges belonging to a critical network. Nevertheless, specific threshold values can be selected based on specific analyses, e.g., depending on the bridge structural typology and including, for example, information on the deck slenderness.

As an example, Figure 7-5 shows flags activation according to the first criteria for a single bridge located in Mantova, i.e., in which a vertical velocity larger than the selected threshold is obtained in the west portion.

Figure 7-5 Example of activated flags at pixel level for a bridge located north of Mantova.

As a final step, an upscaling procedure is performed bridge-by-bridge activating a flag if for each bridge at least one of its grid pixels has an activated flag. Figure 7-6 shows a view of the whole POC corridor indicating in red the bridges with a flag activated.

According to such upscaling approach, out of the total dataset of 480 bridges, about 200 bridges show at least one flag for the last criteria (i.e., a significant percentage difference for two adjacent time windows), 65 bridges show the activation of a flag related to velocities along LOS higher that the threshold of 4 mm/yr, while 31 bridges show the activation of a flag related to reaching the threshold for vertical and/or east-west components of velocities.

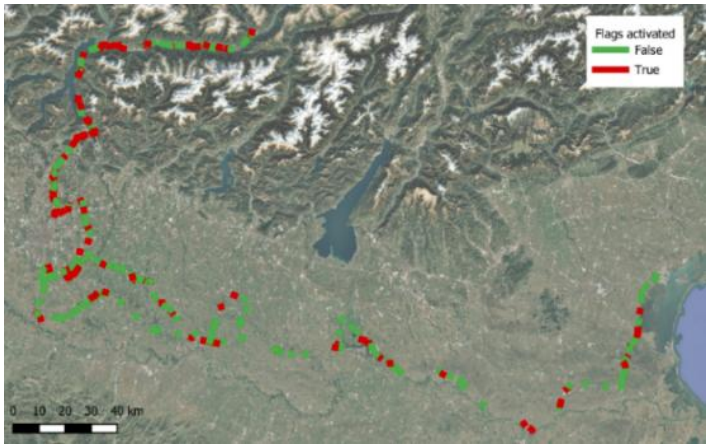

Figure 7-6 Flag activation for each considered bridge belonging to the POC2-1 corridor.

7.3.2 POC 2-2: SS51 Alemagna Roadway

7.3.2.1 Sensitivity Analysis on Bridge Discretization Grid

With reference to the POC2-2 Alemagna case study application, a sensitivity analysis concerning the discretization grid was first performed.

Accordingly, the parametric discretization of bridge footprint showed the strong influence of the assumptions for MPs clustering. Results from the two adopted procedures discussed in §7.2 are compared in Figure 7-7 andFigure 7-8. Namely:

i) On one hand, the first approach (i.e., 30 × 30 m cross-section grid, without subdivision along the longitudinal axis of the bridge) allows for a generally higher density of measurement points (MPs) per tile (Figure 7-7a). Specifically, nearly 70% of the tiles contain at least 4 MPs. However, approximately 20% of the tiles still exhibit a number of MPs equal to 0 or 1, which is insufficient for computing standard deviation of data.

ii) On the other hand, the second approach suffers from a general low density of MPS per tile (Figure 7-8a). Indeed, about 35% of tiles are empty, while only 30% of the tiles are populated with at least 4 MPs.

Nevertheless, while the first approach provides more robust statistics due to the higher MP density per tile, it may fail to capture and highlight displacement patterns that exhibit spatial variability along the deck, particularly in the transverse direction. This limitation can hinder the identification of differential motion phenomena that may be critical for structural assessment.

An example of such a case is shown for a viaduct in Figure 7-7b andFigure 7-8b.

The monitored viaduct exhibits different values of mean velocity along the LOS between the right side (mountain side) and the left side (valley side) of the deck. These differential displacements – which would be worth of further investigation through higher-resolution monitoring data – cannot be detected when using a coarser discretization scheme.

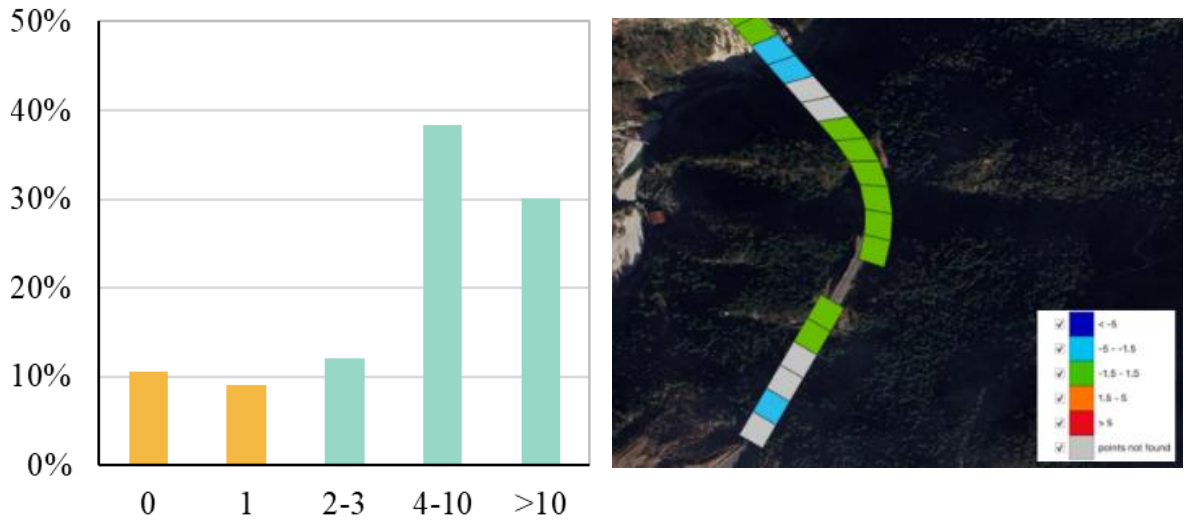

Figure 7-7 Sensitivity to bridge discretization – 30 × 30 m cells, Undivided cross-section grid: a) number of MPs per tile; b) mean velocity per each cell [mm/year].

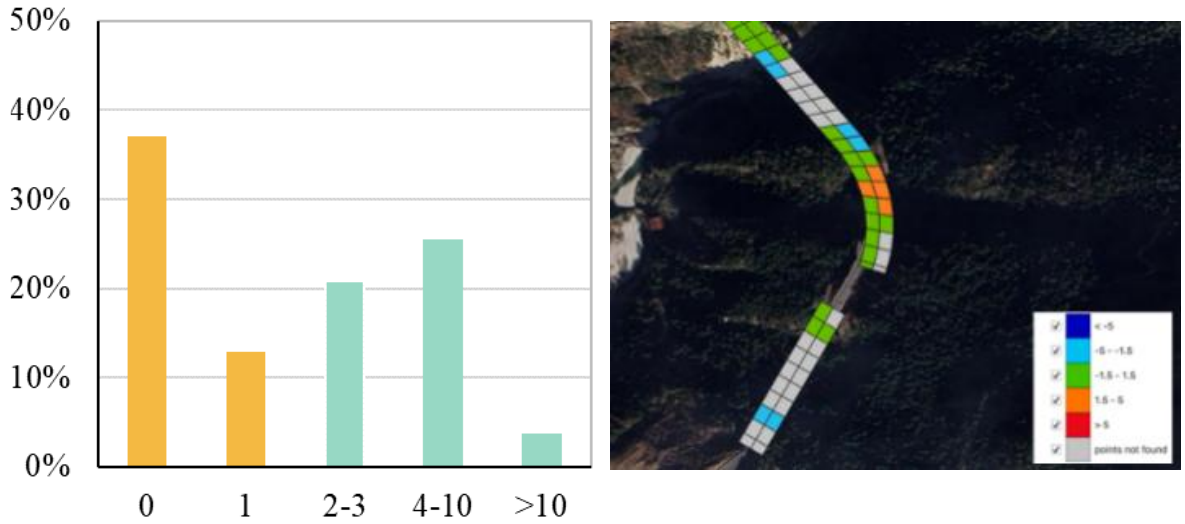

Figure 7-8 Sensitivity to bridge discretization – 20 × 20 m cells, Subdivided cross-section grid: a) number of MPs per tile; b) mean velocity per each cell [mm/year].

7.3.2.2 Sensitivity Analysis Across Orbits and Time Windows

To assess the potential of EGMS data for large-scale infrastructure monitoring, a sensitivity analysis across orbits and time windows was hence performed, i.e., focusing on a stock of 19 bridges with varying lengths and structural typologies.

For each bridge, a linear arrangement of 30 × 30 m cells centred along the bridge axis was assumed, i.e., allowing to compute the average PS' LOS velocity for each cell, resulting in a total of 49 cells across all bridges.

This sensitivity analysis involved two concurring aspects. Firstly, the influence of different EGMS datasets is investigated. To this end, it is worth reporting that in the EGMS archive multiple satellite orbits often cover the same area; for POC2-2 case study, three datasets were considered: Ascending 044 (Asc044), Ascending 117 (Asc117), and Descending 095 (Dsc095). The variation in terms of resulting distribution of LOS velocity was hence assessed for these datasets.

The second level of analysis concerned the temporal consistency of velocity estimates, i.e., by comparing two distinct time windows: 2018–2022 and 2019–2023. EGMS portfolio is updated each year, i.e., allowing to track changes in velocity over time. Such velocity values are calculated as the slope of the best-fitting line through the displacement time series; acceleration is hence estimated as the difference between the velocities computed in the two time-windows.

Table 7-1 summarises the number of populated cells available for each orbit and period, and the number of cells consistently populated across both windows, showing differences among datasets.

Table 7-1 – Number of populated cells per EGMS dataset and time window.

Time Window	**EGMS Dataset**		
	Asc044	Asc117	Dsc095
2018-2022	32	40	33
2019-2023	34	36	31
2018-2022/2019-2023	30	35	29

Figure 7-9 presents the distributions of LOS velocities for each orbit and time window, further highlighting the variability across datasets. To facilitate interpretation of results, Figure 7-9c displays the LOS velocities normalized by the cosine of the incidence angle, i.e., providing an estimate of vertical displacement under the assumption of negligible horizontal motion. However, LOS displacements derived from different orbits do not always yield consistent results, suggesting the need for cross-orbit integration.

Figure 7-9d-f depicts accelerations computed for each orbit as the difference between velocity values across the two time-windows. The results indicate that while most cells exhibit stable velocities over time, those associated with the tails of the distributions, i.e., potentially reflecting anomalous structural behaviour or inconsistencies in the data which require further attention.

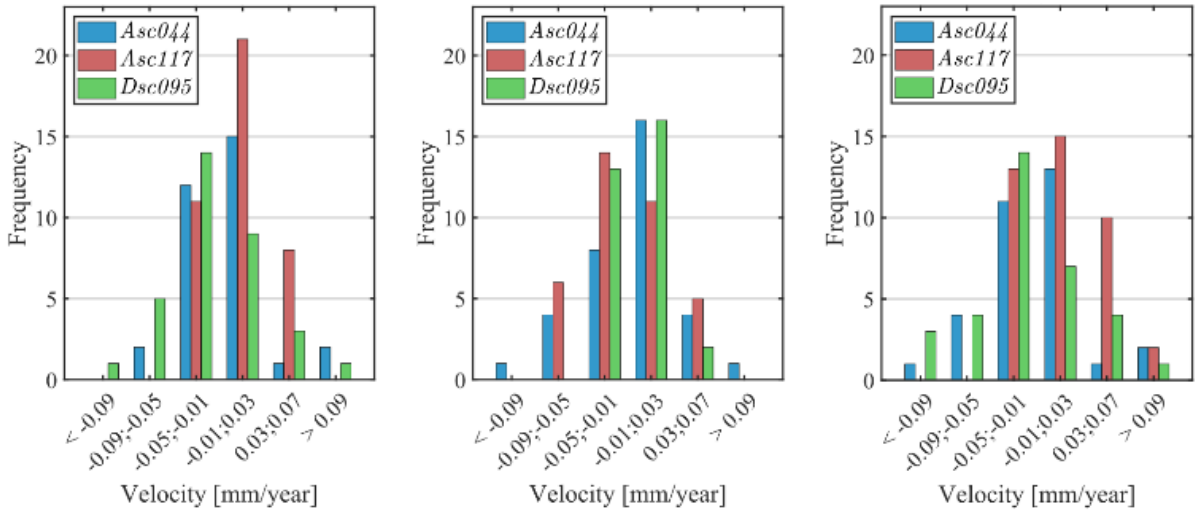

a) b) c)

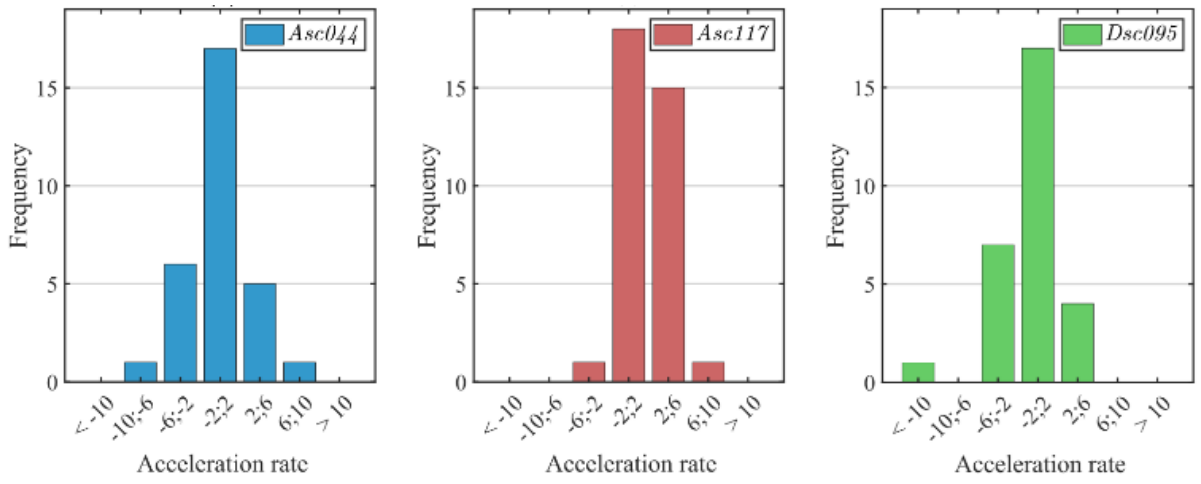

d) e) f)

Figure 7-9 Key analyses results: (a–b) Histograms of LOS velocity values for the 2018–2022 and 2019–2023 time windows, respectively; (c) Estimated vertical displacements; (d–f) Acceleration values derived from differences in LOS velocities between the two time windows for Asc044, Asc117, and Dsc095, respectively.

7.3.3 POC2-3 Calabria Tyrrhenian coastline networks

Results obtained with the methodology described in §7.2 for POC2-3 are depicted in Figure 7-10 with reference to two application cases: *i*) the first one (Figure 7-10a) demonstrates sufficient coverage of east/vertical displacement measurements, while *ii*) the second one highlights poor coverage (Figure 7-10b), thereby reinforcing the rationale for also leveraging single-geometry LOS measurements.

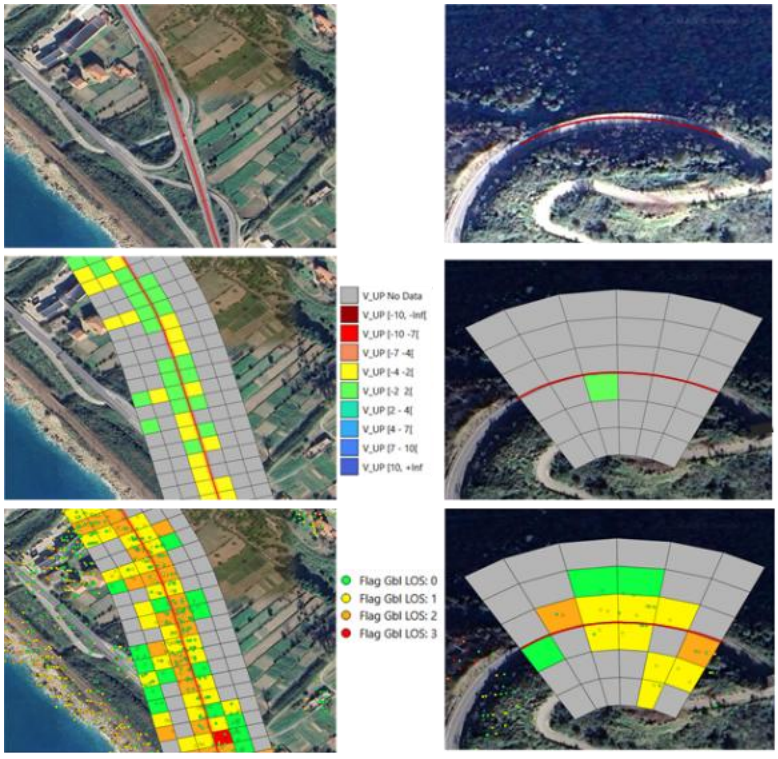

a) b)

Figure 7-10 Application of the methodology proposed for POC2 in two different scenarios: a) sufficient coverage and b) poor coverage in terms of displacement measures.
Top row: orthophoto with the road infrastructure to be monitored;
Middle row: vertical velocity field in 20 m cells, with superimposed sparse PS measurements;
Bottom row: global flag results rasterized on the same 20 m grid, with overlapping PS points.

An example of computed S, V, A, and D flags, i.e., rasterized over 20 m cells for a sufficiently covered infrastructure segment is depicted in Figure 7-11. This example highlights the importance of monitoring not only linear kinematic behavior, such as the average velocity over the entire observation period, but also non-linear trends, including recent variations in displacement velocity during the last year.

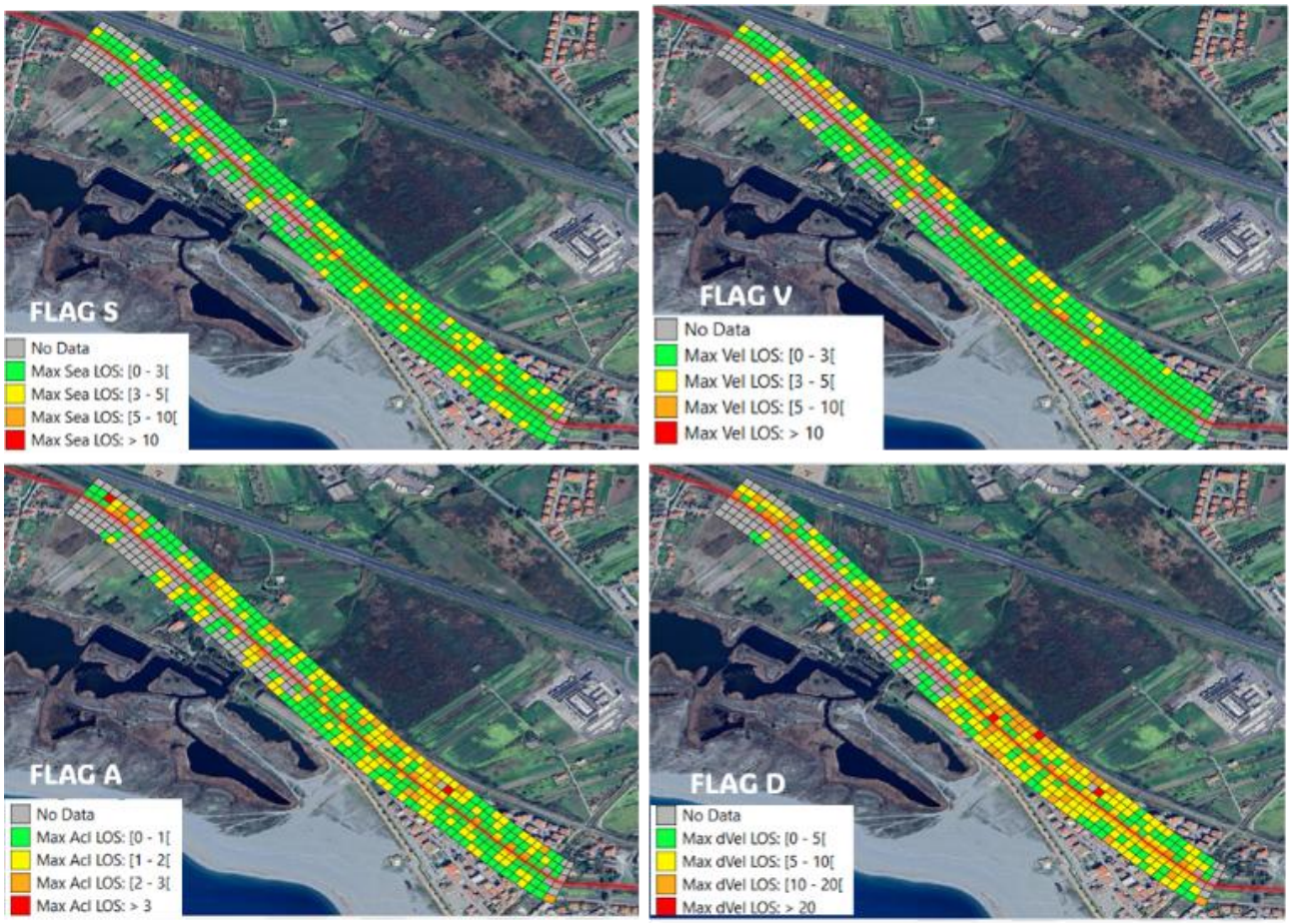

Figure 7-11 Example of cell-based computation of S, V, A, D flags.

Finally, Figure 7-12 highlights how the proposed point-wise flagging methodology enables the identification of specific hot spots exhibiting critical displacement behavior.

In the depicted example, a PS within a cell flagged with the highest severity ($Flag_G = 3$ – Figure 7-12a) displays a clear accelerating displacement trend over time (Figure 7-12b).

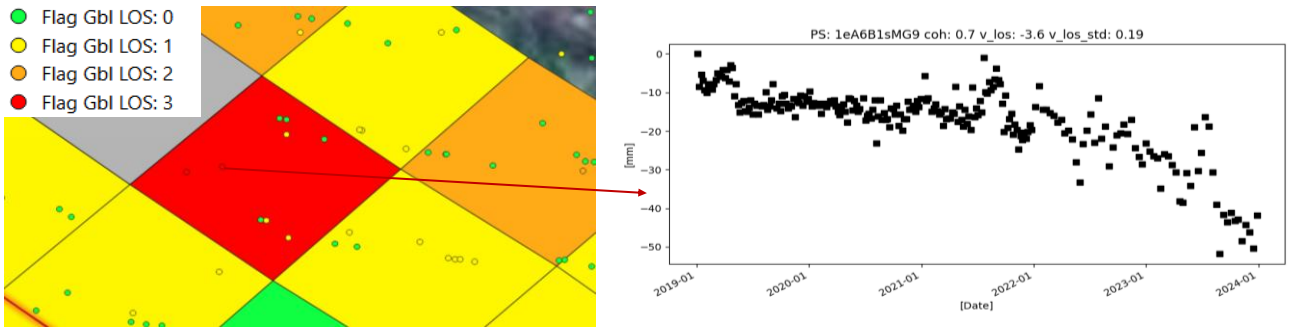

a) b)

Figure 7-12 a) Example of global flag computation, showing both the flagged 20 m cells and the individual PS overlaid, b): Displacement time series of a PS located within a cell flagged with maximum severity, illustrating a clear non-linear deformation trend.

7.4 Visualization of the results through WebGIS platform

The results derived from the application of MT-InSAR techniques described in the previous Sections have been implemented and made accessible through a dedicated WebGIS platform designed to support the monitoring and management of transport CIs.

This platform acts as the primary interface for visualizing and interacting with processed displacement data, enabling the transformation of complex satellite-derived outputs into actionable geo-analytical information. Its development, based on open-source technologies – i.e., specifically the GeoNode framework – ensures both flexibility and scalability, while supporting the integration of diverse spatial data sources.

Within this environment, MT-InSAR displacement datasets are ingested, processed, and rendered through an intuitive map interface, allowing users to explore the spatial and temporal dynamics of ground deformation at both regional and infrastructure-specific scales. The platform hosts a centralized spatial database where georeferenced outputs – such as LOS displacement rates, horizontal and vertical average velocity, maximum velocity and acceleration detected over each segment of infrastructures (e.g., bridges) – as obtained by the application of the methodologies described in the previous Sections, are systematically stored and updated.

Through an interactive geo-portal, i.e., shown in Figure 7-13a, users can access these datasets via thematic maps and analytical dashboards. A set of custom-designed widgets enables the visualization of key indicators previously described, such as average displacement velocity, acceleration trends, and signal stability.

These metrics are crucial for assessing the structural health of transport infrastructure, particularly in hydro-geologically sensitive areas affected by landslides, subsidence, seismicity, or flood-related instabilities [45-46]. A core feature of the platform is the exploitation of the automated classification of infrastructure elements based on the ground motion measurements (PS/DS). Each segment of monitored infrastructure is divided into elementary cells and assigned a synthetic geo-analytic indicator called the Inspection Priority Score (IPS – Figure 7-13b).

This score is obtained through the combined analysis of velocity, differential velocity, acceleration, and seasonality of PS located over these elementary cells. Higher values of the IPS correspond to a greater urgency for field inspection. The elementary cells are thematized in a four-color scheme based on the IPS: *i*) green indicates stable behavior; *ii-iii*) yellow and orange denote infrastructures that require ongoing monitoring to assess their kinematic evolution; *iv*) red flags segments requiring a field inspection with a higher level of priority, with grey identifying areas lacking ground motion measurements. The IPS, based on the parameters described above represents a prioritisation criterion, enabling stakeholders to allocate inspection resources more efficiently [47-48].

In addition to real-time visualization, the platform supports automated reporting functionality. Users can generate infrastructure-specific reports that summarize kinematic behaviour over time. These reports offer detailed insights into long-term deformation patterns, facilitating diagnostic interpretation and maintenance planning.

Furthermore, filtering and querying tools allow users to isolate infrastructure elements based on specific risk attributes, such as IPS thresholds, displacement magnitudes, or administrative boundaries. This capacity for targeted exploration supports risk stratification and enhances situational awareness.

In operational terms, the WebGIS platform serves as a scalable and transferable tool that can be adapted to various geographic and infrastructural contexts. Its modular architecture allows for the integration of additional data layers – such as traffic load, structural health monitoring sensors, or climate datasets – enabling multi-criteria assessments and cross-domain analyses.

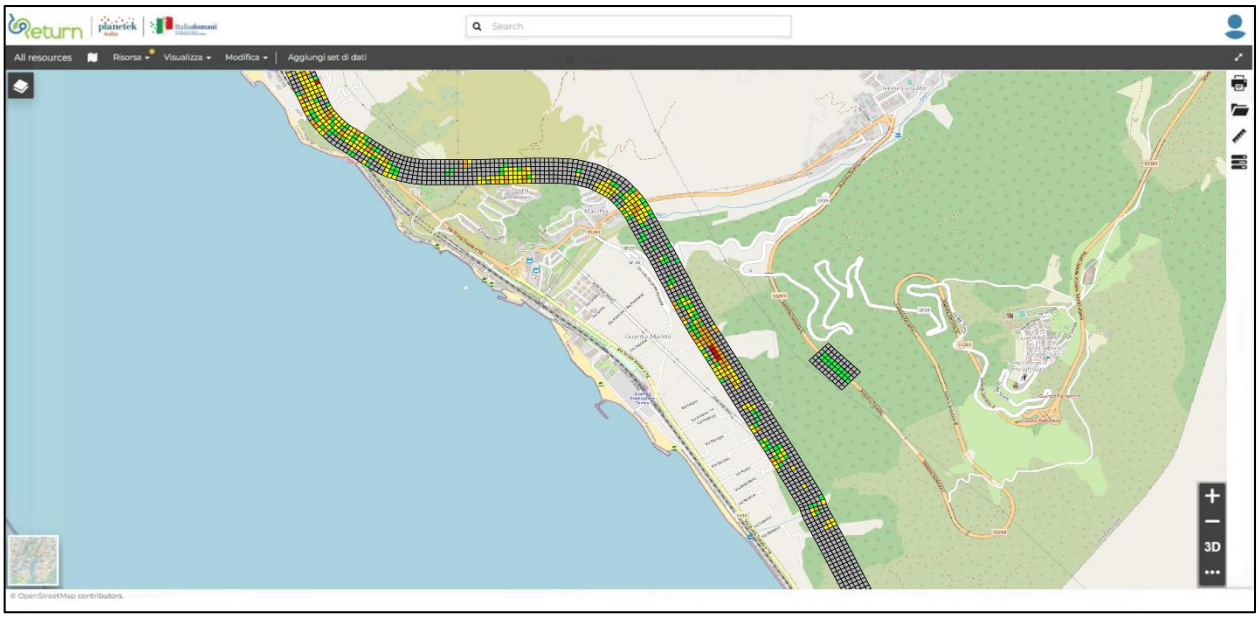

a)

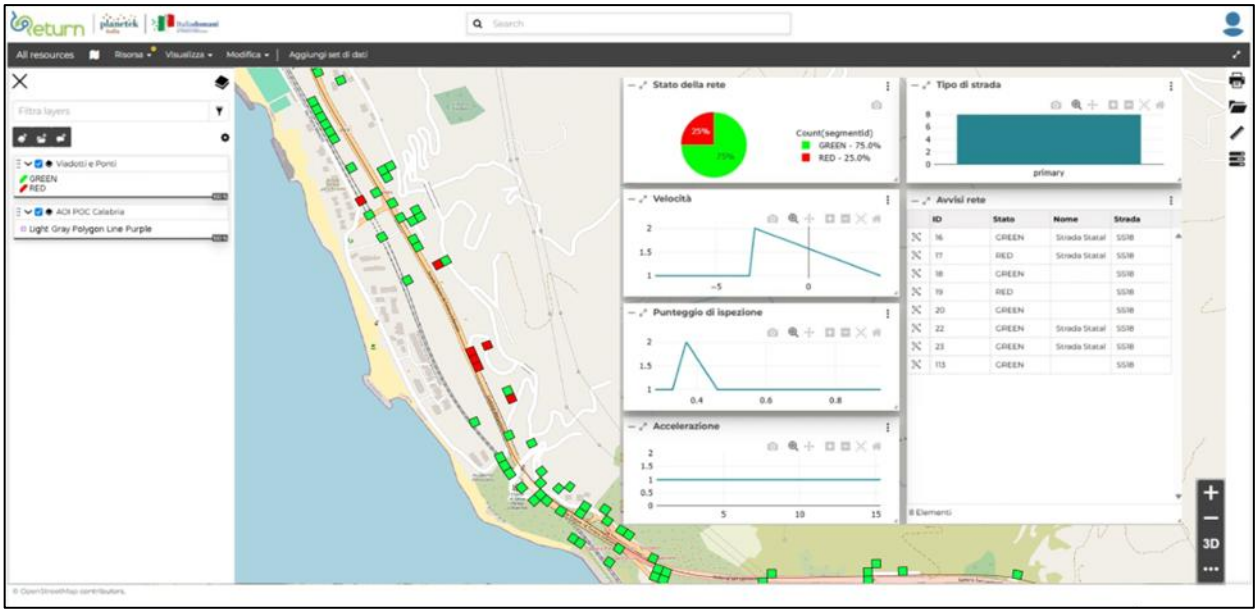

b)

Figure 7-13 a) Interface of the WebGIS platform; b) interactive tools for visualizing and querying road and bridge segments, color-coded according to their assigned Inspection Priority Score.

This flexibility is critically relevant in the context of climate change adaptation, i.e., where the interaction between environmental pressures and infrastructure vulnerability must be continuously reassessed. Moreover, the system's compatibility with standardized geospatial data formats and interoperability protocols (e.g., OGC services) facilitates its integration within broader national or regional spatial data infrastructures (SDIs).

By fostering collaborative data sharing among institutions, operators, and civil protection agencies, the platform supports a more holistic and coordinated approach to risk-informed asset management. Remarkably, the platform enables continuous and updated monitoring of infrastructure segments, highlighting those that show anomalous or accelerating displacement trends.

These critical areas are clearly visualized within the geoportal, reinforcing the platform's function as both a diagnostic and decision-support tool. Delivering a unified environment for data integration, visualization,

classification, and reporting, the system facilitates a comprehensive understanding of infrastructure behavior under dynamic environmental conditions.

Beyond the domain of transport infrastructure, the platform also represents an asset for broader environmental and territorial monitoring, supporting the detection of ground instability, urban subsidence, and hydrogeological hazards across diverse spatial scales [49-50]. This approach contributes significantly to the proactive maintenance and resilience of national transport networks, aligning with broader strategies for sustainable infrastructure development and disaster risk reduction.

7.5 Conclusive remarks of this Section

In this Section, large-scale methodologies for the preliminary structural assessment of critical bridge networks using satellite-derived deformation data have been thoroughly discussed and applied to three different POCs developed within the EP RETURN Project (POC2-1: Tirano-Milano-Marghera, POC2-2: SS51 Alemagna, POC2-3: Calabria Tyrrhenian Coastline), i.e., utilizing MT-DInSAR measurements from both ascending and descending orbits.

By analyzing displacement trends of the measure points, the methodology proposes a risk classification for bridges. This classification can help stakeholders identify the most vulnerable bridges and develop more targeted monitoring and maintenance strategies.

The implemented analyses at territorial scale of roadway and railway networks involved the definition of a geo-referred grid corresponding to the footprint of each structure. The implemented bridge discretization then allows the clustering of Measurement Points (MPs). Different, rapid methodologies to preliminary assess the safety of networks of bridges were hence successfully derived, and relevant results were represented within a freely available, user-friendly WebGIS platform.

8. Insights about integration of In-SAR and on-site monitoring data

8.1 Examples of strategies for data integration

On the basis of the large-scale techniques discussed in the previous Section, most critical bridges within CI networks can be identified and analyzed at a deeper scale, i.e., through suitable integration of In-SAR and on-site monitoring data. In the following, useful insights about such integration approaches are reported, i.e., also on the basis of a systematic review of recent and relevant literature works.

In the first instance, a proper integration of in-situ and space-borne data should first rely on parameters for which a direct correlation is achievable, e.g., displacement measures and – more in general – result from static monitoring.

In this regard, spatial averaging techniques discussed in previous Sections play a key role in providing a consistent data integration. As previously mentioned, suitable corner deflector devices can be placed in critical points to supplement the bridge's own reflection characteristics. A relevant example of application of such expedient is reported in Selvakumaran et al. [51], which monitored a four-span masonry arch bridge over the river Thames trough InSAR and automated total station (ATS) measurements (Figure 8-1).

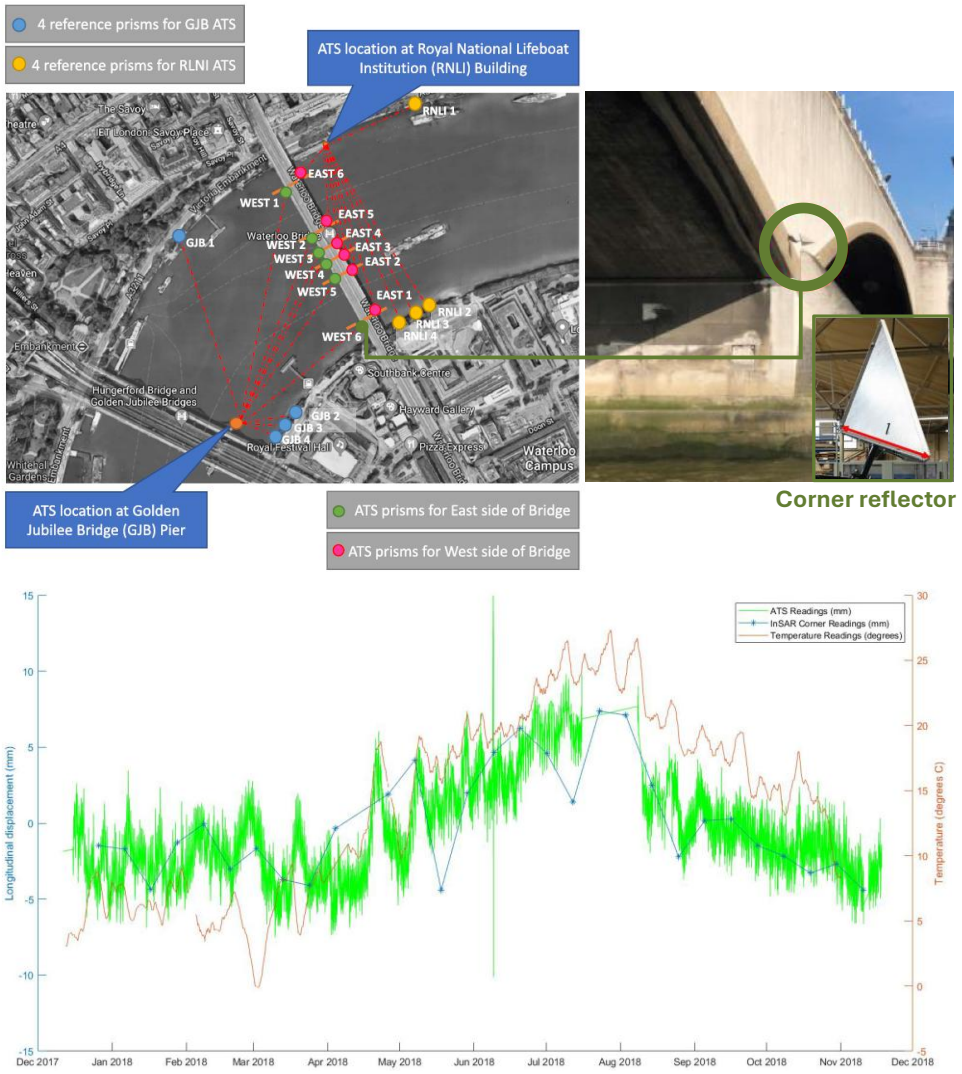

Figure 8-1 Example of ATS-environmental-InSAR data integration for an arch bridge located in London (adapted from [51]).

As shown by the Authors, when plots of ATS and SAR-derived longitudinal movements are compared with temperature readings over time, a good match is achieved, i.e., with SAR readings over the year matching the overall temperature profile and agreeing with the ATS readings.

Nevertheless, point-by-point comparison still resulted in deviation between the readings, i.e., with an ATS-SAR correlation coefficient in the range 0.41-0.76. This surely shows that measures are positively correlated, to a reasonably strong degree. More in detail, a better correlation was achieved in the beginning part of the time period considered, while the two sets of values deviated from each other in the period among May and October. The Authors ascribed such discrepancy to possible phase unwrapping error.

Nevertheless, the above example shows how satellite measurements can be efficiently used to supplement in-situ measurements. In this case, SAR data helped validating ATS measurements and resolving the unknown total station positions and other unknown quantities, giving a better insight into the absolute movements of the bridge (rather than the relative measurements derived from the lone ATS data).

The Authors also performed another relevant example of integration among LVDT-InSAR displacement measures [52] with reference to a second bridge located in London, i.e., featuring a 16-span reinforced concrete structure with balanced cantilever scheme (Figure 8-2).

In this case, combination of satellite and on-site measurements was performed to address seasonal thermal expansion phenomena – on the basis of data from a time window covering years 2011-2018 – resulting in a very good agreement of results. This highlighted once again the potential of integrating data from multiple sources while emphasizing currently open challenges concerning the proper isolation of signals of interest for consistent correlation and subsequent understanding of the bridge performance.

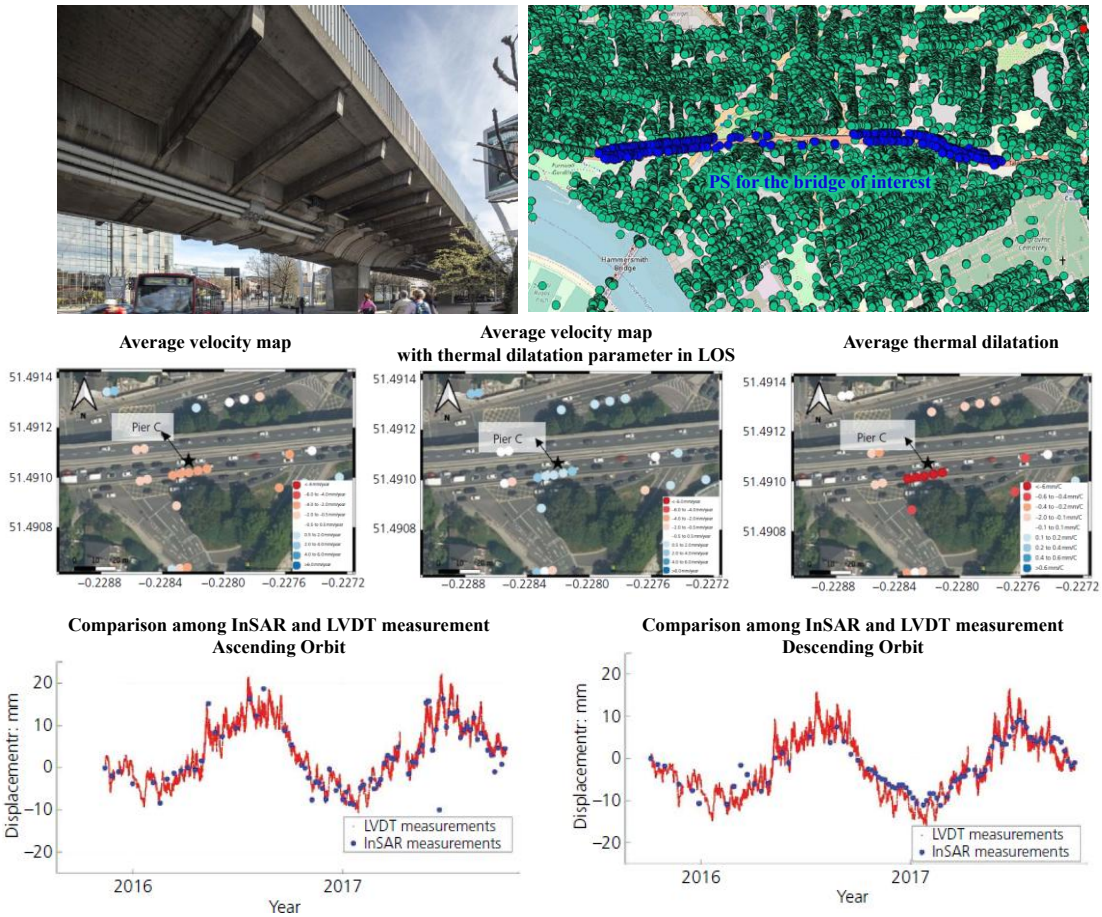

Figure 8-2 Example of LVDT-InSAR data integration to address seasonal thermal expansion phenomena for a reinforced concrete bridge located in London (adapted from [52]).

An open field of research within the framework of damage detection on the basis of in-situ + InSAR measurements is instead represented by the combination of space-borne techniques and terrestrial dynamic monitoring.

To this end, it is worth to preliminarily mention that this kind of approach cannot – in principle – rely on direct correlations between monitored parameter, and hence results should be either qualitatively correlated or more deeply interpreted through the aid of a refined numerical model.

Still, this proved to be a very promising option worth of further investigations. Indeed, on one hand, space-borne measurements can provide information about the long-term deformation of both the structure and the surrounding soil, i.e., enabling to first distinguish among territorial displacement trends (i.e., due to large scale phenomena) and potentially critical, localized deformation phenomena occurring in the bridge. On the other hand, accelerometric and velocimetric data from in-site sensors can be suitably used to monitor structural frequencies and highlight their variation over time. Such variation can be hence linked to structural damage and correlated with anomalous InSAR data trends.

A pioneering example of integration among dynamic in-site and space-borne monitoring is shown in Figure 8-3, which summarizes some results from a three-year long experimental campaign carried out by Ponzo et al. [53].

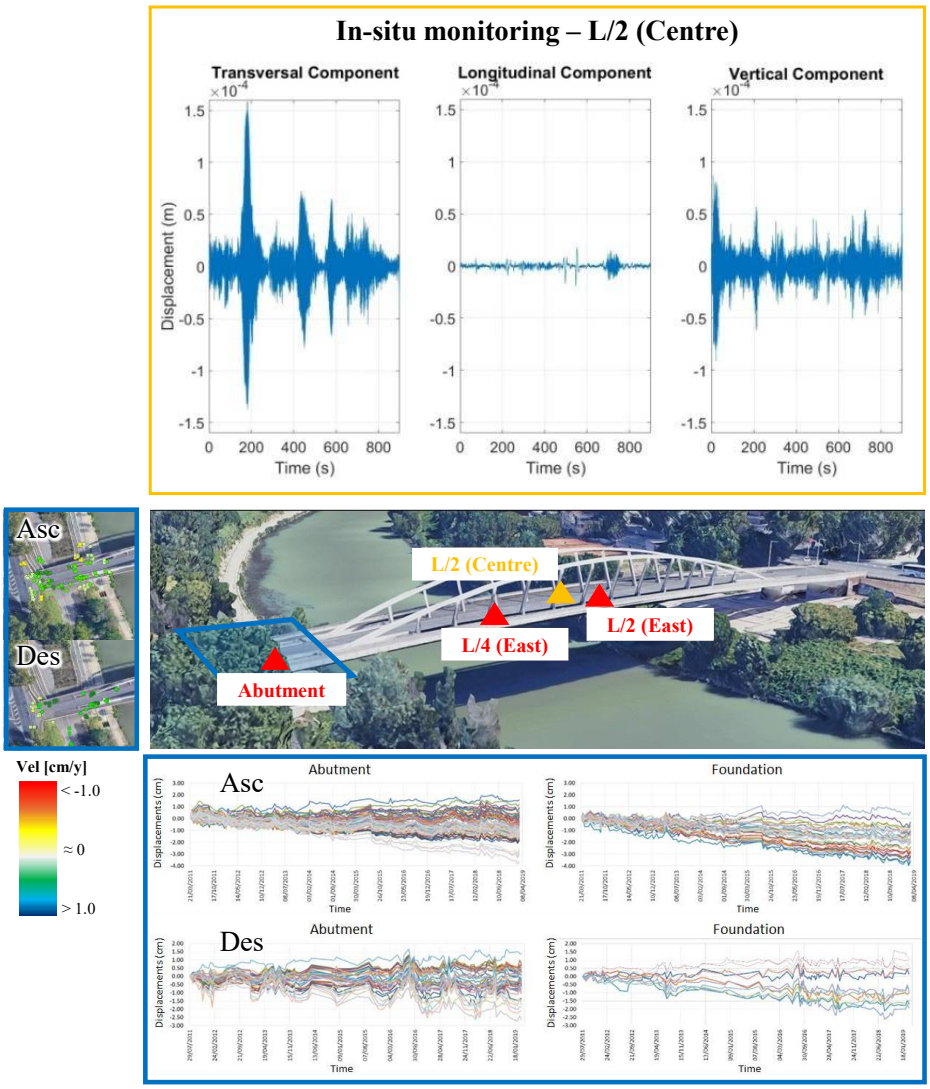

Figure 8-3 Example of dynamic-InSAR data integration for an arch bridge located in Rome (adapted from [53]).

Namely, the Authors selected an upper-way arch bridge crossing the Tiber river as a case study and hence combined results from DIn-SAR monitoring and in-situ velocimetric measures.

The Authors highlighted some non-negligible (linear) trends of lowering of the foundations, which were observed over the time interval 2011–2019. Through combination with in-situ measures – which confirmed the linear elastic behavior of the bridge, with only millimetric and fully reversible inflections due to traffic and wind loads – potential structural damage was ruled out. Settlements were indeed ascribed to the combined consolidation of alluvial deposits and stiff blue clay.

The Authors also confirmed some issues concerning In-SAR monitoring of bridges, i.e., related to the lack of a sufficient number of MPs for highly deformable bridges without riverbed-placed piles. This could represent an even more critical aspect when satellite measures are combined with dynamic monitoring, i.e., due to the aforementioned lack of a direct correlation among measured parameters.

8.2 General design requirements for an SHM system involving on-site and SAR measures

On the basis of relevant methods and examples shown in the previous Sections, it can be clearly inferred that proper design of an integrated SHM system combining in-situ instrumentation and satellite-based InSAR measures requires a multidisciplinary approach, i.e., aimed at ensuring structural safety while balancing computational effort deriving from large dataset processing and relevant analyses accuracy.

As far as possible, the system must be conceived as a unified monitoring architecture, rather than as two independent systems operating in parallel. To this end, the first design step consists in clearly and suitably defining the monitoring objectives and performance requirements. As shown in previous sections, these typically include: *i*) the assessment of global structural behavior through dynamic identification, *ii*) the detection of local damage mechanisms, *iii*) the verification of serviceability LSs, *iv*) the long-term evaluation of progressive displacements, e.g., due to foundation settlements.

To check such performance requirements, physical parameters (accelerations, displacements, rotations, strains at key bridge points – piers, abutments, midspan) and environmental variables (temperature, wind speed, water level when relevant) should be properly evaluated in space and time. Selecting the best technique(s) for such measures should heavily depend on a case-by-case basis, i.e., accounting for bridge structural peculiarities.

Time cadencing of measures should properly account for the relevant resolution deriving from satellite measures. As shown in §7.2 and §7.3, warning thresholds should be established according to multi-level criteria, including instantaneous exceedance (of velocity, acceleration, etc.), scatter of results, and long-term trend evolution.

In-situ sensor network should be designed accounting for expected results from accurate structural analysis, i.e., possibly with the aid of a calibrated FE model of the bridge. Namely, sensor typologies and placement should reflect expected mode shapes and internal actions regimes, i.e., paying particular attention to critical components (piers, bearings, expansion joints, mid-span sections, etc.).

For example, accelerometers can be used for traffic- and wind-based modal identification. Measures should be repeated in time to highlight deviation from the expected behavior that could be related to structural damage, i.e., especially if InSAR-based trends also show non-negligible anomalies. Displacement transducers can be used for monitoring deck and supports movements, while strain gauges can be placed in critical spots for

localized stress/strain evaluations. On the other hand, environmental sensors must be used to compensate thermal effects on a daily and/or seasonal basis, i.e., due to their relevant influence on results which was thoroughly discussed in previous Sections.

The acquisition system must ensure adequate sampling frequency, high-resolution analog-to-digital conversion, and reliable power supply with backup systems. To this end, a robust data storing and transmission infrastructure is also required.

The integration of InSAR data should be performed after accurate georeferencing of CIs, i.e., to ensure consistency between the coordinate systems of ground-based sensors and PSs. Additionally, atmospheric phase delays, orbital inaccuracies, and temporal decorrelation effects must be considered during processing, i.e., as shown in §5 and §6.

Consistent design of the data fusion architecture is essential for an effective integration of each data source. Temporal harmonization strategies should be properly introduce to link high-frequency data streams from in-situ sensors with the discrete acquisition intervals associated with space-borne data. As shown in previous Sections, this can be done through proper aggregated indicators deriving from statistical analysis.

With reference to spatial correlation, great emphasis should be given to PSs aligned with critical bridge components. In order to prevent cases in which measure points are lacking, artificial corner reflectors may designed and installed on-site (i.e., as shown in §8.1).

Calibration and validation procedures should be always first performed to ensure reliability of long-term monitoring. Namely. cross-validation between InSAR and ground-based displacement measurements allows distinction between actual long-term trends and systematic biases.

In conclusion, an effective integrated monitoring system for bridges must combine high-frequency local measures with wide-area and long-term deformation tracking through a unified, model-driven data architecture. Only through coherent temporal and spatial harmonization and robust validation the system can provide reliable support for structural safety assessment and asset management decision-making.

9. Conclusions

In the present deliverable, use of space-borne InSAR data was addressed for SHM of bridges belonging to critical infrastructural networks. For this purpose, different techniques for *i*) manipulation of SAR data, *ii*) SAR-based large scale monitoring and *iii*) integration with on-site measures have been presented, discussed and applied with reference to relevant examples.

For instance, Section 5 dealt with filtering of environmental effects.

For this purpose, the Borgoforte Bridge in Mantua, Italy was selected as a case study. This CI is characterized by a recognized hydraulic risk due to the fluctuating level of the underflowing Po river. Satellite image filtering and inSAR analysis was carried out using data from both the EGMS portal and the COSMO-SkyMed (CSK) satellite constellation. The analysis compared the reconstructed structural displacements obtained from these datasets, discussing their respective strengths and limitations. Namely, while a significant negative correlation among the water level and the SAR-based vertical displacements was identified using EGMS data, CSK data resulted in a non-resolutive outcome due to exceeding scatter. This effect depends on data processing artifacts deriving from ineffective environmental filtering.

Section 6 dealt with suitable statistical models for satellite image analysis. In particular, such models were introduced either with respect to a territorial and a single-structure scale.

Statistical models were used to identify and interpretate structural displacements via the so-called SBAS-DInSAR method (*Small BAseline Subset Differential Interferometry*). Illustrated approaches are based on the mean LOS (*line-of-sight*) velocity, which was hence used to estimate both vertical and E-W direction deformation accounting for the directional cosines of the orbit. Deformation trends can be hence monitored and potentially correlated with environmental causes. With reference to the relevant case of temperature-induced deformations, the Pearson coefficient was shown to be a suitable correlation indicator. Subsequently, seasonal trends were monitored via a moving average metric. Finally, for a deeper analysis of trends recognition, details concerning the AutoRegressive output with an eXogenous input part model (ARX) were also described, i.e., as ARX can be used to develop an automated damage detection system for CIs.

Section 7 addressed large-scale monitoring of critical transportation networks through analysis of InSAR data.

Namely, automated procedures for rapid and yet consistent bridge segmentation were first proposed, i.e., assessing their validity with dedicated sensitivity analyses. Subsequently, the spatial fusion of data deriving from different PSs was addressed, i.e., proposing rapid, flag-based techniques referring to relevant displacement, velocity and/or acceleration threshold. By analyzing time-depending trends of measure points, a large-scale risk classification for bridges was proposed, i.e., aiming at helping stakeholders to identify most vulnerable bridges and develop more targeted monitoring and maintenance strategies. Relevant results were represented within a freely available, user-friendly WebGIS platform.

Finally, Section 8 addressed integration among on-site measures and satellite-based monitoring. As shown in relevant examples, consistent and effective data fusion among terrestrial dynamic, environmental and space-borne monitoring can be obtained, although significant challenges are still present. To this end, some useful insights concerning the design of an integrated SHM system are finally pointed out.

10. References

1. Luo, L.; Wang, X.; Guo, H.; Lasaponara, R.; Zong, X.; Masini, N.; Wang, G.; Shi, P.; Khatteli, H.; Chen, F.; et al. Airborne and Spaceborne Remote Sensing for Archaeological and Cultural Heritage Applications: A Review of the Century (1907–2017). Remote Sens. Environ. 2019, 232, 111280.

2. Macchiarulo, V.; Giardina, G.; Milillo, P.; González Martí, J.; Sánchez, J.; DeJong, M.J. Settlement-Induced Building Damage Assessment Using MT-Insar Data for the Crossrail Case Study in London. In International Conference on Smart Infrastructure and Construction 2019 (ICSIC); ICE Publishing: Cambridge, UK, 2019; pp. 721–727.

3. Tang, P.; Chen, F.; Zhu, X.; Zhou, W. Monitoring Cultural Heritage Sites with Advanced Multi-Temporal InSAR Technique: The Case Study of the Summer Palace. Remote Sens. 2016, 8, 432.

4. Zhou, W.; Chen, F.; Guo, H. Differential Radar Interferometry for Structural and Ground Deformation Monitoring: A New Tool for the Conservation and Sustainability of Cultural Heritage Sites. Sustainability 2015, 7, 1712–1729.

5. Ferretti, A.; Prati, C.; Rocca, F. Permanent Scatterers in SAR Interferometry. IEEE Trans. Geosci. Remote Sens. 2001, 39, 8–20.

6. Berardino, P.; Fornaro, G.; Lanari, R.; Sansosti, E. A New Algorithm for Surface Deformation Monitoring Based on Small Baseline Differential SAR Interferograms. IEEE Trans. Geosci. Remote Sens. 2002, 40, 2375–2383.

7. Lanari, R.; Mora, O.; Manunta, M.; Mallorqui, J.J.; Berardino, P.; Sansosti, E. A Small-Baseline Approach for Investigating Deformations on Full-Resolution Differential SAR Interferograms. IEEE Trans. Geosci. Remote Sens. 2004, 42, 1377–1386.

8. Farneti, E.; Cavalagli, N.; Costantini, M.; Trillo, F.; Minati, F.; Venanzi, I.; Ubertini, F. A Method for Structural Monitoring of Multispan Bridges Using Satellite InSAR Data with Uncertainty Quantification and Its Pre-Collapse Application to the Albiano-Magra Bridge in Italy. Struct. Health Monit. 2023, 22, 353–371.

9. Macchiarulo, V.; Milillo, P.; Blenkinsopp, C.; Giardina, G. Monitoring Deformations of Infrastructure Networks: A Fully Automated GIS Integration and Analysis of InSAR Time-Series. Struct. Health Monit. 2022, 21, 1849–1878.

10. Selvakumaran, S.; Plank, S.; Geiß, C.; Rossi, C.; Middleton, C. Remote Monitoring to Predict Bridge Scour Failure Using Interferometric Synthetic Aperture Radar (InSAR) Stacking Techniques. Int. J. Appl. Earth Obs. Geoinf. 2018, 73, 463–470.

11. Xiong, S.; Wang, C.; Qin, X.; Zhang, B.; Li, Q. Time-Series Analysis on Persistent Scatter-Interferometric Synthetic Aperture Radar (PS-InSAR) Derived Displacements of the Hong Kong–Zhuhai–Macao Bridge (HZMB) from Sentinel-1A Observations. Remote Sens. 2021, 13, 546.

12. Zeni, G.; Bonano, M.; Casu, F.; Manunta, M.; Manzo, M.; Marsella, M.; Pepe, A.; Lanari, R. Long-Term Deformation Analysis of Historical Buildings through the Advanced SBAS-DInSAR Technique: The Case Study of the City of Rome, Italy. J. Geophys. Eng. 2011, 8, S1–S12.

13. Arangio, S.; Calò, F.; Di Mauro, M.; Bonano, M.; Marsella, M.; Manunta, M. An Application of the SBAS-DInSAR Technique for the Assessment of Structural Damage in the City of Rome. Struct. Infrastruct. Eng. 2014, 10, 1469–1483.

14. Zhu, M.; Wan, X.; Fei, B.; Qiao, Z.; Ge, C.; Minati, F.; Vecchioli, F.; Li, J.; Costantini, M. Detection of Building and Infrastructure Instabilities by Automatic Spatiotemporal Analysis of Satellite SAR Interferometry Measurements. Remote Sens. 2018, 10, 1816.

15. Pepe, A.; Lanari, R. On the Extension of the Minimum Cost Flow Algorithm for Phase Unwrapping of Multitemporal Differential SAR Interferograms. IEEE Trans. Geosci. Remote Sens. 2006, 44, 2374–2383.

16. Falabella, F.; Serio, C.; Masiello, G.; Zhao, Q.; Pepe, A. A Multigrid InSAR Technique for Joint Analyses at Single-Look and Multi-Look Scales. IEEE Geosci. Remote Sens. Lett. 2022, 19, 1–5.

17. Ojha, C.; Manunta, M.; Lanari, R.; Pepe, A. The Constrained-Network Propagation (C-NetP) Technique to Improve SBAS-DInSAR Deformation Time Series Retrieval. IEEE J. Sel. Top. Appl. Earth Obs. Remote Sens. 2015, 8, 4910–4921.

18. Bonano, M.; Manunta, M.; Marsella, M.; Lanari, R. Long-Term ERS/ENVISAT Deformation Time-Series Generation at Full Spatial Resolution via the Extended SBAS Technique. Int. J. Remote Sens. 2012, 33, 4756–4783.

19. Di Carlo, F.; Miano, A.; Giannetti, I.; Mele, A.; Bonano, M.; Lanari, R.; Meda, A.; Prota, A. On the Integration of Multi-Temporal Synthetic Aperture Radar Interferometry Products and Historical Surveys Data for Buildings Structural Monitoring. J. Civ. Struct. Health Monit. 2021, 11, 1429–1447.

20. Casu, F.; Manzo, M.; Lanari, R. A Quantitative Assessment of the SBAS Algorithm Performance for Surface Deformation Retrieval from DInSAR Data. Remote Sens. Environ. 2006, 102, 195–210.

21. Bonano, M.; Manunta, M.; Pepe, A.; Paglia, L.; Lanari, R. From Previous C-Band to New X-Band SAR Systems: Assessment of the DInSAR Mapping Improvement for Deformation Time-Series Retrieval in Urban Areas. IEEE Trans. Geosci. Remote Sens. 2013, 51, 1973–1984.

22. Talledo, D.A.; Miano, A.; Bonano, M.; Di Carlo, F.; Lanari, R.; Manunta, M.; Meda, A.; Mele, A.; Prota, A.; Saetta, A.; et al. Satellite Radar Interferometry: Potential and Limitations for Structural Assessment and Monitoring. J. Build. Eng. 2022, 46, 103756.

23. Manunta, M.; De Luca, M.; Zinno, I.; Casu, F.; Manzo, M.; Bonano, M.; Fusco, A.; Pepe, A.; Onorato, G.; Berardino, P.; et al. The Parallel SBAS Approach for Sentinel-1 Interferometric Wide Swath Deformation Time-Series Generation: Algorithm Description and Products Quality Assessment. IEEE Trans. Geosci. Remote Sens. 2019, 57, 6259–6281.

24. Bonaldo, G.; Caprino, A.; Lorenzoni, F.; da Porto, F. Monitoring Displacements and Damage Detection through Satellite MT-InSAR Techniques: A New Methodology and Application to a Case Study in Rome (Italy). Remote Sens. 2023, 15, 1177. https:// doi.org/10.3390/rs15051177

25. Shepard, D. A Two-Dimensional Interpolation Function for Irregularly-Spaced Data. In Proceedings of the 1968 23rd ACM National Conference; Association for Computing Machinery: New York, NY, USA, 1968; pp. 517–524.

26. QGIS.org QGIS User Guide—QGIS Documentation. Available online: https://docs.qgis.org/3.22/en/docs/user_manual/index.html

27. Floris, M.; Fontana, A.; Tessari, G.; Mulè, M. Subsidence Zonation Through Satellite Interferometry in Coastal Plain Environments of NE Italy: A Possible Tool for Geological and Geomorphological Mapping in Urban Areas. Remote Sens. 2019, 11, 165.

28. Di Traglia, F.; De Luca, C.; Manzo, M.; Nolesini, T.; Casagli, N.; Lanari, R.; Casu, F. Joint Exploitation of Space-Borne and Ground-Based Multitemporal InSAR Measurements for Volcano Monitoring: The Stromboli Volcano Case Study. Remote Sens. Environ. 2021, 260, 112441.

29. Coccimiglio, S.; Coletta, G.; Lenticchia, E.; Miraglia, G.; Ceravolo, R. Combining Satellite Geophysical Data with Continuous On-Site Measurements for Monitoring the Dynamic Parameters of Civil Structures. Sci. Rep. 2022, 12, 2275.

30. Lorenzoni, F.; Caldon, M.; da Porto, F.; Modena, C.; Aoki, T. Post-Earthquake Controls and Damage Detection through Structural Health Monitoring: Applications in l'Aquila. J. Civ. Struct. Health Monit. 2018, 8, 217–236.

31. Lee Rodgers, J.; Nicewander, W.A. Thirteen Ways to Look at the Correlation Coefficient. Am. Stat. 1988, 42, 59–66.

32. Hair, J.F.; Black, W.C.; Babin, B.J.; Anderson, R.E.; Tatham, R.L. Multivariate Data Analysis, 7th ed.; Pearson Education Limited: Harlow, UK, 2014; ISBN 978-1-292-02190-4.

33. Swinscow, T.D.V.; Campbell, M.J. Statistics at Square One, 10th ed.; BMJ: London, UK, 2002; ISBN 1-280-19790-0.

34. Johnston, F.R.; Boyland, J.E.; Meadows, M.; Shale, E. Some Properties of a Simple Moving Average When Applied to Forecasting a Time Series. J. Oper. Res. Soc. 1999, 50, 1267.

35. Hansun, S. A Novel Research of New Moving Average Method in Time Series Analysis. Int. J. New Media Technol. IJNMT 2014, 1, 22.

36. Hyndman, R.J.; Athanasopoulos, G. Forecasting: Principles and Practice, 2nd ed.; OTexts: Heathmont, Australia, 2018; ISBN 978-0-9875071-1-2.

37. Huber-Carol, C.; Balakrishnan, N.; Nikulin, M.S.; Mesbah, M. Goodness-of-Fit Tests and Model Validity; Birkhäuser: Boston, MA, USA, 2002; ISBN 978-1-4612-6613-6.

38. Wald, A. Statistical Decision Functions. Nature 1951, 167, 1044.

39. Akaike, H. Fitting Autoregressive Models for Prediction. Ann. Inst. Stat. Math. 1969, 21, 243–247.

40. Miano, A., Mele, A., Silla, M., Bonano, M., Striano, P., Lanari, R., ... & Prota, A. (2025). Space-borne DInSAR measurements exploitation for risk classification of bridge networks. Journal of Civil Structural Health Monitoring, 15(3), 731-744.

41. Mele, A., Crosetto, M., Miano, A., & Prota, A. (2023). ADAfinder tool applied to EGMS data for the structural health monitoring of urban settlements. Remote Sensing, 15(2), 324.

42. Talledo, D.A.; Saetta, A. A Multi-Level Semi-Automatic Procedure for the Monitoring of Bridges in Road Infrastructure Using MT-DInSAR Data. Remote Sens. 2025.

43. Teatini, P., et al. (2011), Geomechanical response to seasonal gas storage in depleted reservoirs: A case study in the Po River basin, Italy, J. Geophys. Res., 116, F02002, doi:10.1029/2010JF001793

44. J. Wasowski, et al. (2022), Chapter 11 - Remote sensing of landslide motion with emphasis on satellite multi-temporal interferometry applications: an overview, Editor(s): Tim Davies, Nick Rosser, J.F. Shroder, In Hazards and Disasters Series, Landslide Hazards, Risks, and Disasters (Second Edition), Elsevier, 2022, Pages 365-438, ISBN 9780128184646, https://doi.org/10.1016/B978-0-12-818464-6.00006-8.

45. Al Hudaib, H. T., & Ray, R. P. (2023). The Methodologies and Main Challenges of Assessment the Multi-Hazard Interaction and Risk Management Associated with Roads Infrastructures and Dam Safety: A Review. International Journal of Integrated Engineering, 15(7), 174-188.

46. Frattini, P., Crosta, G. B., & Allievi, J. (2013). Damage to buildings in large slope rock instabilities monitored with the PSInSAR™ technique. Remote sensing, 5(10), 4753-4773. https://doi.org/10.3390/rs5104753

47. Crosetto, M., Monserrat, O., Cuevas-González, M., Devanthéry, N., & Crippa, B. (2016). Persistent scatterer interferometry: A review. ISPRS Journal of Photogrammetry and Remote Sensing, 115, 78-89. https://doi.org/10.1016/j.isprsjprs.2015.10.011

48. Nettis, A., Massimi, V., Nutricato, R., Nitti, D. O., Samarelli, S., & Uva, G. (2023). Satellite-based interferometry for monitoring structural deformations of bridge portfolios. Automation in Construction, 147, 104707. https://doi.org/10.1016/j.autcon.2022.104707

49. Aiello, A., Massimi, V., Taggio, N., Borrelli, R., Laurino, V., Filippi, E., ... & Casucci, M. (2023, December). A Land Monitoring Service for Local Public Administrations: The IRIDE EOS4LPA Lot 3 Project. In Italian Conference on Geomatics and Geospatial Technologies (pp. 99-108). Cham: Springer Nature Switzerland.

50. Kushabaha, A., Capolongo, D., Scicchitano, G., Rizzo, F., & Zingaro, M. (2025). Sediment flow connectivity index data for the Apulia region (Italy): An open-source geodatabase and the innovative CONNECTOSED WebGIS platform. Data in Brief, 58, 111210.

51. Ponzo, F.C., Iacovino, C., Ditommaso, R., Bonano, M., Lanari, R., Soldovieri, F., Cuomo, V., Bozzano, F., Ciampi, P., Rompato, M. (2021). Transport Infrastructure SHM Using Integrated SAR Data and On-Site Vibrational Acquisitions: "Ponte Della Musica–Armando Trovajoli" Case Study. Applied Sciences, 11, 6504.

52. Selvakumaran, S., Rossi, C., Marinoni, A., Webb, G., Bennetts, J., Barton, E., Plank, S., Middleton, C. (2020). Combined InSAR and Terrestrial Structural Monitoring of Bridges. IEEE Transactions on Geoscience and Remote Sensing, 58, 7141-7153.

53. Selvakumaran, S., Sadeghi, Z., Collings, M., Rossi, C., Wright, T., Hooper, A. (2021). Comparison of in situ and interferometric synthetic aperture radar monitoring to assess bridge thermal expansion. Proceedings of the Institution of Civil Engineers - Smart Infrastructure and Construction, 175(2), 73-91.